REVISTA BRASILEIRA DE CIÊNCIAS MECÂNICAS

JOURNAL OF THE BRAZILIAN SOCIETY OF MECHANICAL SCIENCES

REVISTA BRASILEIRA DE CIÊNCIAS MECÂNICAS
JOURNAL OF THE BRAZILIAN SOCIETY OF MECHANICAL SCIENCES

PREDICTION OF OPTIMUM GEOMETRY, AND THE PERFORMANCE OF VALVELESS PULSED COMBUSTORS IN GAS TURBINES, USING A MATHEMATICAL MODEL

UM MODELO MATEMÁTICO PARA A OBTENÇÃO DA GEOMETRIA ÓTIMA E DO DESEMPENHO DE QUEIMADORES PULSATIVOS SEM VÁLVULA EM TURBINAS À GÁS

J.A. Olorunmaiye
Dept. of Mech. Eng.
University of Ilorin
Ilorin, Nigeria

J.A.C. Kentfield
Dept. of Mech. Eng.
The University of Calgary
Calgary, Alberta, Canada, T2N 1N4

ABSTRACT

A mathematical model of valveless pulsed combustors, in which the effects of chemical reaction were considered, is presented. The flows in the inlet and tail pipe were assumed to be one-dimensional whilst the combustion chamber was treated as a large reservoir with uniform thermodynamic properties. The set of hyperbolic partial differential equations obtained were solved by a numerical method of characteristics. The model was used to study the effects of changes in combustor geometry, and intake pressure and temperature on the performance of the combustor. The model shows that shortage of fresh air in the combustion chamber is what degrades the performance of the pulsed combustor when the geometry employed differs from the optimum one. The results obtained also show that pulsation amplitude in the combustion chamber, a parameter for assessing the performance of pulsed combustor, increases with intake pressure whereas it decreases with intake temperature. It is also established that an optimum performance of valveless pulsed combustor can be obtained in gas turbine application, if there is intercooling between the compressor and the pulsed combustor.

Keywords: Valveless Pulsed Combustors ■ Combustion Chamber ■ Method of Characteristics ■ Gàs Turbine Application

RESUMO

Um método matemático de queimadores pulsativos sem válvula é apresentado em que os efeitos da reação química são considerados. Os fluxos na entrada e no tubo de saída são considerados unidimensionais enquanto que a câmara de combustão foi tratada como um grande reservatório com propriedades termodinâmicas uniformes. O conjunto de equações diferenciais parciais hiperbólicas obtido foi resolvido pelo método numérico de características. O modelo foi utilizado para estudar os efeitos das mudanças na geometria dos queimadores, da pressão na entrada e da temperatura no desempenho do queimador. O modelo mostra que a diminuição de ar na camara de combustão é o fator de degradação do desempenho do queimador pulsativo quando a geometria utilizada difere daquela ótima. Os resultados obtidos mostram também que a amplitude de pulsação na camara de combustão, parâmetro para acessar-se o desempenho do queimador pulsativo, aumenta com a pressão na entrada enquanto diminui com a temperatura na entrada. Também conclui-se do presente trabalho que um desempenho ótimo do queimador pulsativo sem válvula pode ser obtido nas aplicações de turbinas à gás se houver um sistema de refrigeração integrado entre o compressor e o queimador pulsativo.

Palavras-chave: Queimadores Pulsativos sem Válvula ■ Câmara de Combustão ■ Método de Características ■ Aplicações em Turbinas à Gás

NOMENCLATURE

Roman Letters

Symbol	Nondimensional form	Meaning
a	$A = a/a_0$	Speed of sound
B, E, F, H, Y		Group of terms defined after equation (11)
C_i		Mass fraction of the i-th species
C_f		Friction Factor
C_p	$C_p' = C_p/R_0$	Specific heat of gas mixture at constant pressure
C_{p_i}	$C_{p_i}' = C_{p_i}/R_0$	Specific heat of the i-th species at constant pressure
C_v	$C_v' = C_v/R_0$	Specific heat of gas mixture at constant volume
C_{v_i}	$C_{v_i}' = C_{v_i}/R_0$	Specific heat of the i-th species at constant volume
d		Duct diameter
E		Acitivation energy
E_{cc}	$E_{cc}' = E_{cc}/\rho_0 l_0^3 R_0 T_0$	Internal energy of combustion chamber content
f_i		Mole fraction of the i-th species
g_i	$G_i = g_i l_0/a_0$	Rate of production of the i-th species per unit mass of the gas mixture
h	$h' = h/R_0 T_0$	Enthalpy per unit mass
H, M, O, T		Feet of characteristics (see Figures 2 and 3)
h_c		Convective heat transfer coefficient
I, J, L, M, N, V		Grid points (see Figures 2 and 3)

K		Reaction rate constant
l_0		Reference length
m_{cc}	$M_{cc} = m_{cc}/\rho_0 l_0^3$	Mass of combustion chamber
$\dot{m}$	$\dot{M} = \dot{m}/\rho_0 l_0^3 a_0$	Mass flow rate
$\dot{m}_f'''$		Mass of fuel consumed per unit volume in a unit time
N	N	Number of species
P	$P' = P/P_0$	Pressure
q	$Q' = q l_0/a_0^3$	Heat transfer rate per unit mass
Q		Heat transfer rate
R	$R' = R/R_0$	Specific gas constant of gas mixture
R_i	$R_i' = R_i/R_0$	Specific gas constant of i-th species
R_u		Universal gas constant
s	$S = s/R_0$	Specific entropy
t	$Z = t a_0/l_0$	Time
T	$T' = T/T_0$	Temperature
U	$U = u/a_0$	Velocity
w	$W = w l_0/a_0^2$	Frictional force per unit mass
x	$X = x/l_0$	Axial distance

Greek Letters

α	$\alpha' = \alpha/l_0^2$	Area
$\gamma = C_p/C_v$		Ratio of specific heat
Δt	ΔZ	Time step size
Δx	ΔX	Spatial grid size
ε		Emissivity
ρ	$D = \rho/\rho_0$	Density
σ		Stefan-Boltzmann constant

Subscripts

| cc | | Combustion chamber |

e_1	Left end of the inlet
e_2	Right end of the inlet
e_3	Left end of the tail pipe
e_4	Right end of the tail pipe
f	Fuel
f_i	Internal energy, or enthalpy, or entropy of formation of the i-th species per unit mass
g	Gas
H, O, T	Feet of characteristics (See Figures 2 and 3)
HV	Along line HV (See Figures 2 and 3)
in	Inner wall surface
max	Maximum
min	Minimum
OV	Along line OV (See Figures 2 and 3)
R	Reference pressure or temperature for the definition of enthalphy, internal energy, and change in entropy
TV	Along line TV (See Figures 2 and 3)
V	Grid point V (See Figures 2 and 3)
w	Wall
O	Reference quantity; Ambient air

Superscripts

$'$	Normalized with respect to appropriate reference value
Z	Time Z
$Z + \Delta Z$	Time $Z + \Delta Z$

INTRODUCTION

A pulsed combustor, by design, operates with combustion-driven oscillation which was once usually considered a nuisance and even sometimes a danger [1] in practical combustion systems. Increasing interest is being shown in the application of pulsed combustors because of their ability to operate with gain in stagnation pressure [2], enhanced convective heat transfer to the wall [3], and reduced NO_x formation [4]. Domestic heating units in which pulsed combustors are used are currently being marketed under the trade name LENNOX PULSE FURNANCE. Work is being done to develop pulsed combustor for gas turbine application [5].

Pulsed combustors of so many different geometries have been built by various inventors. The inlet of the combustor may be equipped with valves or it may be valveless, the inlet, in that case, being designed to function as an aerodynamic valve. The geometry of the pulsed combustor on which this work was done, the valveless SNECMA-Lockwood Type, is shown in Figure 1.

A disadvantage of pulsed combustors which has militated against their development is the difficulty of studying them theoretically due to the complexities of their working processes. This has resulted in a situation whereby workers have relied almost exclusively on experimental cut-and-techniques to optimize the geometry of pulsed combustors. Servanty [6] reported that SNECMA, a French aero-engine manufacturer, built and tested several thousand different configurations of valveless pulsed combustors between 1943 and 1971.

Due to the realization of the advantages of good theoretical simulation as a cost-effective means of predicting the effect of design changes, several workers have attempted to model the operation of the pulsed combustor mathematically. Marzouk [7] developed an isentropic cold flow model to simulate the operation of the SNECMA-Lockwood combustor. The combustion process was replaced by a simulated instantaneous injection of air resulting in a peak combustion chamber pressure measured experimentally. Cronje [8] extended this model to include the effect of heat transfer and friction. However, the assumptions of flow separation in the tail pipe and constant-reaction-rate combustion occuring sequentially instead of concurrently with charging/discharging process in the combustion chamber, minimised the confidence with which the model could be
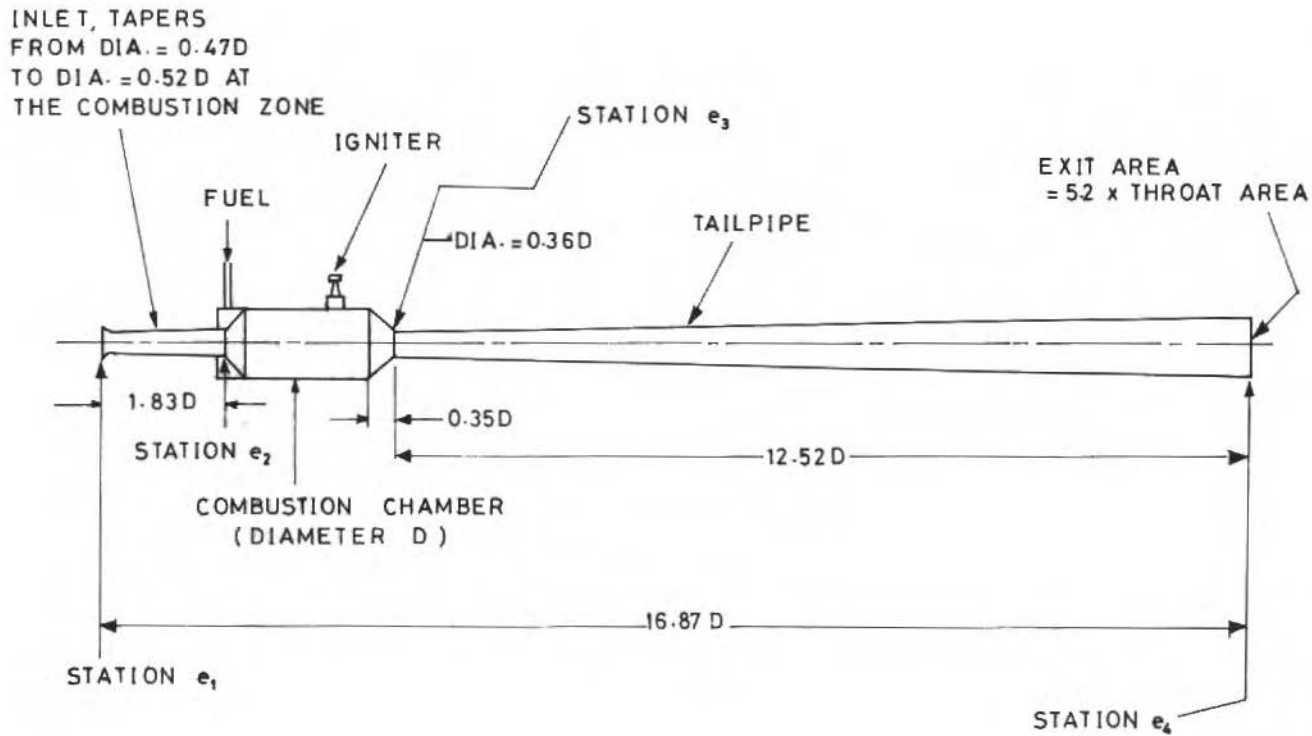
Figure 1. Proportions of a SNECMA-Lockwood valveless pulsed combustor.

J.A. Olorunmaiye and J.A.C. Kentfield

applied as an optimizing tool. Clarke and Craigen [9] modelled the operation of an organ pipe pulsed combustor using a simple overall reaction rate equation. This model could not be used as a predictive tool due to the requirements of wall temperature distribution along the combustor and pressure-time variation at the left end of the combustor as part of the data input.

This paper describes a model which was developed to overcome the shortcomings mentioned above so that it can be used as an optimization tool for the geometry of valveless pulsed combustors.

MATHEMATICAL MODEL

Inlet and Tail Pipe

Assuming the flows in the inlet and tail pipe to be quasi-one-dimensional, and neglecting molecular diffusion, longitudinal viscous and conductive effect, the conservation equations for mass, momentum, energy and species are:

$$\frac{1}{\rho}\frac{D\rho}{Dt} + \frac{\partial u}{\partial x} + u\frac{d\ln\alpha}{dx} = 0 \tag{1}$$

$$\frac{Du}{Dt} + \frac{1}{\rho}\frac{\partial P}{\partial x} + w = 0 \tag{2}$$

$$\frac{Dh}{Dt} - \frac{1}{\rho}\frac{DP}{Dt} = q + uw \tag{3}$$

$$\frac{DC_i}{Dt} = g_i \qquad (i = 1, 2, \ldots N - 1) \tag{4}$$

The chemical source function for each species

$$g_i = g_i(P, \rho, C_1, \ldots C_{N-1}) \tag{5}$$

can be determined from the chemical reactions taking place in the flow.

The specific enthalpy and entropy are given by

$$h = h(P, \rho, C_1, \ldots C_{N-1}) \tag{6}$$

and

$$s = s(P, \rho, C_1, \ldots C_{N-1}) \tag{7}$$

The gas mixture is assumed to be a perfect gas and

$$P = \rho RT \tag{8}$$

where $R = \sum_{i=1}^{N} C_i R_i$ and

$$h = C_p(T - T_R) + \sum_{i=1}^{N} C_i h_{f_i} \tag{9}$$

where $C_p = \sum_{i=1}^{N} C_i C_{p_i}$

Using equations (6) and (7) in equation (3) and substituting for the partial derivatives and nondimensionalizing the resulting equations, the following can be obtained:

$$\frac{\partial P'}{\partial Z} + U \frac{\partial P'}{dX} + \gamma_c DA^2 \frac{\partial U}{dX} = -\gamma_0 DA^2 F + E - B \tag{10}$$

$$\frac{DS}{DZ} = H + Y \tag{11}$$

where

$$B = \sum_{i=1}^{N} G_i \left\{ \frac{DR'}{C_v'} [C_{p_i}'(T' - T_R') + h_{f_i}'] - \frac{p' \gamma R_i'}{R'} \right\}$$

$$E = \frac{\gamma_0 (Q' + UW) DR'}{C_v'}$$

$$F = U \frac{d\ln\alpha}{dX}$$

$$H = -C'_v \sum_{i=1}^{N} G_i \left\{ \left[\ln \left(\frac{DT'_R R'}{P'_R} \right) \left(\frac{C'_{p_i}}{C'_v} - \frac{C'_{v_i}}{C'_v} \right) \right. \right.$$

$$- \frac{S_{f_i}}{C'_v} - \frac{C'_{v_i}}{C'^2_v} \left(S - \sum_{i=1}^{N} C_i \, S_{f_i} \right) + \frac{R'_i}{C'_v} \ln f_i$$

$$- \frac{C'_{v_i}}{C'_v} \ln \prod_{i=1}^{N} f_i^{c_i R_i / C'_v} + \frac{DR' h_i}{p' C'_v} \right\}$$

$$Y = \frac{\gamma_0 R' D}{P'} \left(Q' + UW \right)$$

The nondimensional forms of equations (2) and (4) are

$$\frac{1}{\gamma_0 D} \frac{dP'}{\partial X} + \frac{\partial U}{\partial Z} + U \frac{\partial U}{\partial X} = -W \tag{12}$$

and

$$\frac{DC_i}{DZ} = G_i \tag{13}$$

$(i = 1, 2, \ldots, N - 1)$

Equations (10)–(13) constitute a set of quasi-linear hyperbolic partial differential equations which were solved using the method of characteristics. In this method, a rectangular grid is imposed on the integration domain and the equations are integrated along the characteristics directions. The dependent variables used are $P', U, S, C_1, C_2, \ldots C_{N-1}$. Following the procedure given by by Courant and Hilbert [9] the characteristic curves and compatibility equations were derived. The characteristics having reciprocal slopes $(U + A)$, $(U - A)$ and U are labelled OV, TV, and HV respectively, see Figure 2. The finite difference approximation of the compatibility equations are:

$$U_V - U_0 + \frac{1}{\gamma_0} \left(\frac{1}{DA} \right)_{OV} (P'_V - P'_o) = -\left(AF + W + \frac{B - E}{\gamma_0 DA} \right)_{OV} \Delta Z \tag{14}$$

$$U_V - U_T - \frac{1}{\gamma_0} \left(\frac{1}{DA} \right)_{TV} (P'_V - P'_T) = -\left(-AF + W + \frac{E - B}{\gamma_0 DA} \right)_{TV} \Delta Z \tag{15}$$

$$S_V = S_H + (H + Y)_{HV} \, \Delta Z \tag{16}$$

$$C_{i_V} = C_{i_H} + G_{i_{HV}} \ \Delta Z \tag{17}$$

$(i = 1, 2, \ldots, N - 1)$.

The double subscripts on a term indicates that the term is taken to be mean of its value at the end points indicated by the two subscripts.

(a) Subsonic Flow to the Right   (b) Supersonic Flow to the Right

(c) Subsonic Flow to the Left   (d) Supersonic Flow to the Left
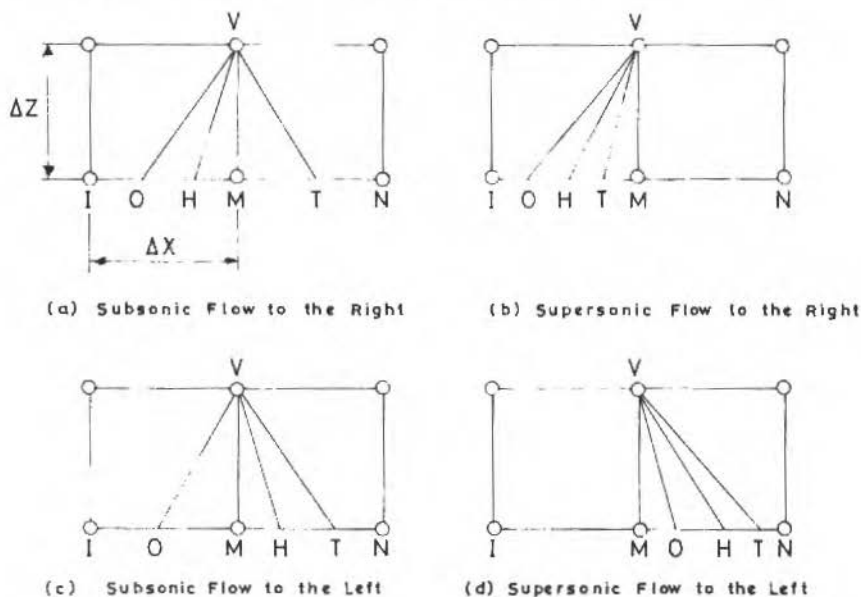
Figure 2. The characteristics reaching and internal grid point.

Combustion Chamber

Treating the combustion chamber as a control volume, it is assumed that the thermodynamic properties of the gas mixture in the combustion chamber are uniform and that the mixture has homogeneous composition. Neglecting molecular diffusion into or out of the combustion chamber, the finite difference approximation of the combustion chamber equantions are

$$M_{cc}^{Z+\Delta Z} = M_{cc}^{Z} + \left(D_{e_2} \alpha'_{e_2} U_{e_2} - D_{e_3} \alpha_{e_3} U_{e_3} + \dot{M}_f \right)^z \Delta Z \tag{18}$$

$$E_{cc}'^{Z+\Delta Z} = E_{cc}'^{Z} + \left[D_{e_2} \alpha_{e_2}' \ U_{e_2} \left(h_{e_2}' + \frac{U_{e_2}^2}{2} \right) - \right.$$
$$\left. D_{e_3} \alpha_{e_3}' U_{e_3} \left(h_{e_3}' + \frac{U_{e_3}^2}{2} \right) + M_f C_{p_f}' \ T_f' + M_{cc} \ Q' \right]^Z \Delta Z \qquad (19)$$

$$C_{i_{cc}}^{Z+\Delta Z} = \left[\left(C_{i_{cc}} M_{cc} \right)^Z + \left(D_{e_2} \ C_{i_{e_2}} \ \alpha_{e_2}' \ U_{e_2} - D_{e_3} \ C_{i_{e_3}} \ \alpha_{e_3}' \ U_{e_3} \right. \right.$$
$$\left. \left. + G_{i_{cc}} \ M_{cc} \right)^Z \ \Delta Z \right] \Big/ M_{cc}^{Z+\Delta Z} \qquad (20)$$

$(i = 1, 2, \ldots, N - 1)$.

Boundary Condition

The velocities at the inlet and tail pipe boundaries may be positive or negative. The flow was assumed to be quasi-steady at the boundaries of the inlet and tail pipe. Rudinger [10] reported that results obtained from this assumption for the kind of boundaries being considered in this work are in good agreement with experimental observations.

Inflow through any bonundary was assumed to be isentropic since the effect of the factors that cause entropy increase (such as friction, mixing and combustion) between the limit of the flow source (ambient air or combustion chamber) and the boundary grid point, was expected to be small compared with the effect of these factors in the pipes (inlet or tail pipe). Therefore, the entropy at the grid point was the same as that of the flow source (ambient air or the combustion chamber). The mass fractions of the species at the boundary grid point were the same as those of the species in the flow source. Since the flow was assumed to be quasi-steady, the steady flow energy equation and the compatibility equation of the characteristic reaching the boundary were solved to obtain the remaining dependent variables. The characteristics reaching boundary grid points for different flow velocities are shown in Figure 3.
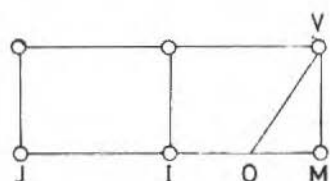
(a) Subsonic Inflow at the Right End
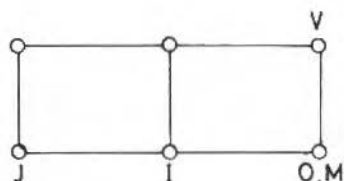
(b) Sonic Inflow at the Right End
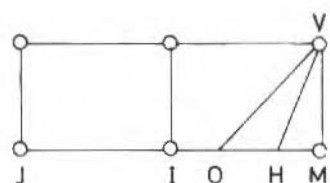
(c) Subsonic Outflow at the Right End
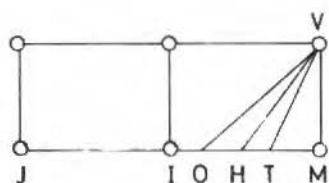
(d) Supersonic Outflow at the Right End
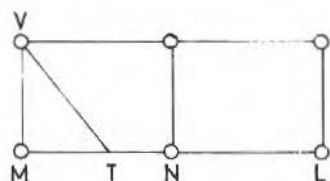
(e) Subsonic Inflow at the Left End
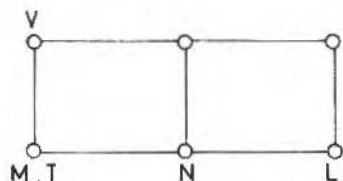
(f) Sonic Inflow at the Left End
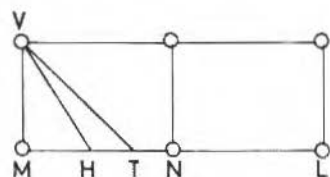
(g) Subsonic Outflow at the Left End
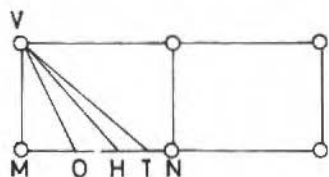
(h) Supersonic Outflow at the Left End

Figure 3. The characteristics reaching boundary grid points.

Since outflow through any boundary was assumed to be quasi-steady, the static pressure at the boundary was the same as that in the space into which discharge took place (the ambient or combustion chamber) if the flow was subsonic. The compatibility equation of the characteristics reaching the boundary were solved to obtain the other dependent variables.

In the case of sonic/supersonic outflow, all the characteristics are washed sownstream and the dependent variables at the boundary were obtained by solving the compatibility equations of all the characteristics.

Combustion Model

Assuming complete oxidation of the fuel (propane), the following overall reaction equation was used:

$$\dot{m}_f''' = K \ C_{C_3H_8}^{1.5} \ C_{O_2}^{0.5} \ \rho^2 \exp[-E/R_u T] \tag{21}$$

The values of activation energy and reaction rate constant used are $E = 30 \ MJ$/kmol and $K = 4.5 \times 10^6 \ m^3$/kg.s.

Heat Transfer and Wall Friction

The rate of heat transfer by convection and radiation from the wall is

$$Q = h_c \ \alpha_{in}(T_w - T_g) + \frac{\varepsilon_w + 1}{2} \ \sigma\varepsilon_g \ \alpha_{in}(T_w^4 - T_g^4) \tag{22}$$

The frictional force per unit mass on the fluid element at the grid is

$$w = \frac{4C_f}{d} \ u|u| \tag{23}$$

C_f and h_c were obtained using equations of the forms relating friction factor and Nusselt number to local flow parameters in steady flow. Gas emissitivity ε_g was taken to be 0.04. This value was calculated from experimentally determined gas and wall temperatures [11].

Initial Conditions

The flow in the pulsed combustor is cyclic unsteady flow. At the beginning of the first cycle, the combustion chamber was assumed to be filled with air at pressure $P'_A + 0.5$) and temperature $(T'_A + 3.5)$ while the inlet and tail pipe were assumed to be filled with air at ambient conditions. The combustion model was brought in, in the second cycle. By the 15th cycle the operation of the combustor had converged to a cyclic operation.

Stability Criterion

The time step was chosen in accordance with the Courant-Friedrichs-Lewy stability criterion [12] which requires that

$$\Delta Z \le \frac{\Delta X}{A + |U|} \tag{24}$$

More detailed description of this mathematical model can be found elsewhere [11,13]. Good results were obtained when the model was applied to predict flows in shock tubes and pulsed combustors. When 41 and 501 grid points were used in the shock tube computation, the improvement of the predicted result with increasing number of grid points was found to be very small — far from being commensurate with the increase in computation time [14].

USE OF THE MODEL AS AN OPTIMIZATION TOOL

The geometries of the inlet, combustion chamber and tail pipe were varied for a fuel flow rate of 7.24 kg/h. The effects of these geometrical changes on the performance of the pulsed combustor were assessed in terms of the pressure range in the combustion chamber, the total static thrust generated at e_1 and e_4, and the average fresh air aspiration rate through the inlet into the combustion chamber. The performance of the combustor with its present geoemtry, which was optimized by experimental cut-and-try technique by earlier workers, are underscored with broken lines in Tables I-VII.

Table I. Variation of combustor performance with combustion chamber, volume change, as predicted with the model for a fuel flow rate of 7.24 kg/h. The geometries of the inlet and tail pipe were held constant.

Combustion chamber volume $\times 10^4$ (m^3)	Nondimensional pressure range in combustion chamber	Total static thrust generated at e_1 and e_4 (N)	Air flow rate from e_2 into combustion chamber kg/h
3.348	0.512	7.68	48.06
5.022	0.992	10.80	112.25
6.714	1.457	31.72	128.49
10.464	1.072	25.68	112.27
13.393	0.688	17.04	81.10

Combustion Chamber

Table I shows the results obtained by varying the combustion chamber volume while freezing the geometries of the inlet and tail pipe. It can be seen that the volume giving optimum performance is indeed the present volume. The reason for the peaking of the performance at the present volume was found to be due to the mass of the fresh air charge inhaled being maximum at this volume.

Inlet Geometry

The length of the inlet and its cross-sectional area at e_2 were varied while freezing the geometries of the combustion chamber and tail pipe. Tables II and III show the results. Again, it can be seen that the present inlet geometry gave the best performance. The poor performance with other geometries was caused by shortage of oxygen in the cobustion chamber due to poor charging.

Table II. Variation of combustor performance with inlet length as as predicted with the model for a fuel flow rate of 7.24 kg/h. Inlet areas at e_1 and e_2, and the geometries of the combustion chamber and tail pipe were fixed.

Inlet Length $\times 10^2$ (m)	Nondimensional pressure range in combustion chamber	Total static thrust generated at e_1 and e_4 (N)	Air flow rate from e_2 into combustion chamber (kg/h)
7.62	0.701	14.06	69.08
12.19	1.197	21.02	124.17
15.24	1.457	31.72	128.49
16.76	1.331	21.38	108.05
22.86	0.772	8.98	51.66
30.48	0.504	6.26	64.14

Table III. Variation of combustor performance with inlet area at e_2 as predicted with the model for a fuel flow rate of 7.24 kg/h inlet length and its divergence angle, and the geometries of the combustion chamber and tail pipe were fixed.

Inlet Area $\alpha e_2 \times 10^3$ (m^2)	Nondimensional pressure range in combustion chamber	Total static thrust generated at e_1 and e_4 (N)	Air flow rate from e_2 into combustion chamber (kg/h)
0.314	0.283	0.94	52.16
0.707	0.740	8.03	44.66
1.131	1.457	31.72	128.49
1.590	0.583	18.90	69.48
1.963	0.598	16.30	78.37

Tail pipe geometry

With the tail pipe areas at e_3 and e_4 fixed, a tail pipe having a length that is shorter than that of the tail pipe used in the present geometry by 76 mm gave slightly better performance than the present geometry as shown in Table IV.

Poor combustion chamber charging was observed when the other tail pipe lengths were used.

Table IV. Variation of combustor performance with tail pipe length as predicted with the model for a fuel flow rate of 7.24 kg/h . Tail pipe areas at e_3 and e_4, and the geometries of the inlet and combustion chamber were fixed.

Pipe Length (m)	Nondimensional pressure range in combustion chamber	Total static thrust generated at e_1 and e_4 (N)	Air flow rate from e_2 into combustion chamber (kg/h)
0.6096	0.551	9.21	35.10
0.8382	1.464	33.90	123.32
0.9144	1.457	31.72	126.49
1.1430	0.441	4.61	48.22
1.4478	0.512	6.61	32.98

Table V. Variation of combustor performance with tail pipe area at e_4 as predicted with the model for a fuel flow rate of 7.24 kg/h . Tail pipe length and its area at e_3, and the geometries of the inlet and combustion chamber were fixed.

Tail Pipe area $\alpha_{e_4} \times 10^3$ (m^2)	Nondimensional pressure range in combustion chamber	Total static thrust generated at e_1 and e_4 (N)	Air flow rate from e_2 into combustion chamber (kg/h)
0.575	1.512	24.09	134.31
3.066	1.457	31.72	128.49
4.748	1.433	38.58	126.11
6.900	1.441	43.46	126.89

Table V shows the effect of variation of tail pipe cross-sectional area at e_4 on the performance of the combustor. For the case with a smaller e_4 area than the present geometry, the combustion chamber fresh air charge was slightly greater

and a higher pressure range was developed. However, the thrust was lower due to the reduced area which resulted in a lower mass flow through e_4 in both directions. With higher areas at e_4, the fresh air charge and the pressure range in the combustion chamber were approximately the same as for the present geometry, but higher thrusts were generated due to larger flow areas at e_4.

The effects of changes in magnitude of the tail pipe area at e_3 on the performance of the combustor can be seen in Table VI. At first, the total thrust generated and the combustion chamber pressure range reduced as the area at e_3 increased. The change in trend observed at an area of $1.59 \times 10^{-3} m^2$ is believed to be due to the pulsed combustor changing its oepration from that of being somewhat like a Schmidt burner due to the closeness of the tail pipe diameter to that of the combustion chamber. At a slightly smaller area of e_3 than in the present geometry, improved performance can be obtained as shown in Table VI.

Table VI. Variation of combustor performance with tail pipe area at e_3 as predicted with the model for a fuel flow rate of 7.24 kg/h   Tail pipe length and its area at e_4, and the geometries of the inlet and combustion chamber were fixed.

Tail Pipe area $\alpha_{e_3} \times 10^3$ (m^2)	Nondimensional pressure range in combustion chamber	Total static thrust generated at e_1 and e_4 (N)	Air flow rate from e_2 into combustion chamber (kg/h)
0.254	1.520	39.37	142.17
0.575	1.457	31.72	128.49
1.590	0.236	4.25	41.72
3.066	0.992	17.32	74.20

In Table VII, the performances of three combustors having uniform diameter tail pipe are compared with the performance of the present geometry. It can be seen that the performance of a pulsed combustor having a diverging tail pipe is indeed superior to that with a uniform diameter tail pipe as reported earlier by Marzouk [7].

Table VII. Variation of performances of pulsed combustors with tail pipe of uniform diameters to that of present geometry.

Dimensions of Tail Pipe			Performance		
$\alpha_{e_3} \times 10^3$ (m^2)	$\alpha_{e_4} \times 10^3$ (m^2)	Length (m)	P' in max Combustion Chamber	P' in min Combustion Chamber	Total Thrust at e_1 and e_4 (N)
0.575	0.575	0.9144	2.307	0.782	24.23
3.066	3.066	0.9144	1.765	0.774	17.35
1.591	1.591	0.9144	1.965	0.792	17.20
0.575	3.066	0.9144	2.234	0.777	31.72

PREDICTING THE EFFECTS OF VARIATION OF INTAKE FLOW TEMPERATURE AND PRESSURE

Imagining that the pulsed combustor was placed in a large reservoir containing air, the pressure or temperature of the air in the reservoir was varied, hypothetically using the numerical model, to see what effect such a variation would have on the operation of the combustor.

Increasing the ambient pressure while keeping the ambient temperature fixed approximately simulates intercooled supercharged operation. Not only did the absolute values of minimum and maximum pressure in the combustion chamber increase with ambient pressure as expected, the pressure amplitude increased as well, see Figure 4. This trend is in agreement with the work of Porter [15] who reported an increase of between 2 and 13% in the pulsation amplitude in the combustion chamber, in his experimental runs of a valveless pulsed combustor at a pressure of 3 atmospheres.

The total thrust generated at e_1 and e_4 and the mass of fresh charge inhaled through e_2 increased with ambient pressure as shown in Figure 5. The improvement in performance with ambient pressure higher than 1.0 was due to an increase in the density of the ambient air which resulted in more oxigen being available for combustion in the combustion chamber.

When the ambient pressure was fixed at 0.75 (a pressure of 66 kPa), the performance of the combustor was poor as can be seen in Figures 4 and 5.
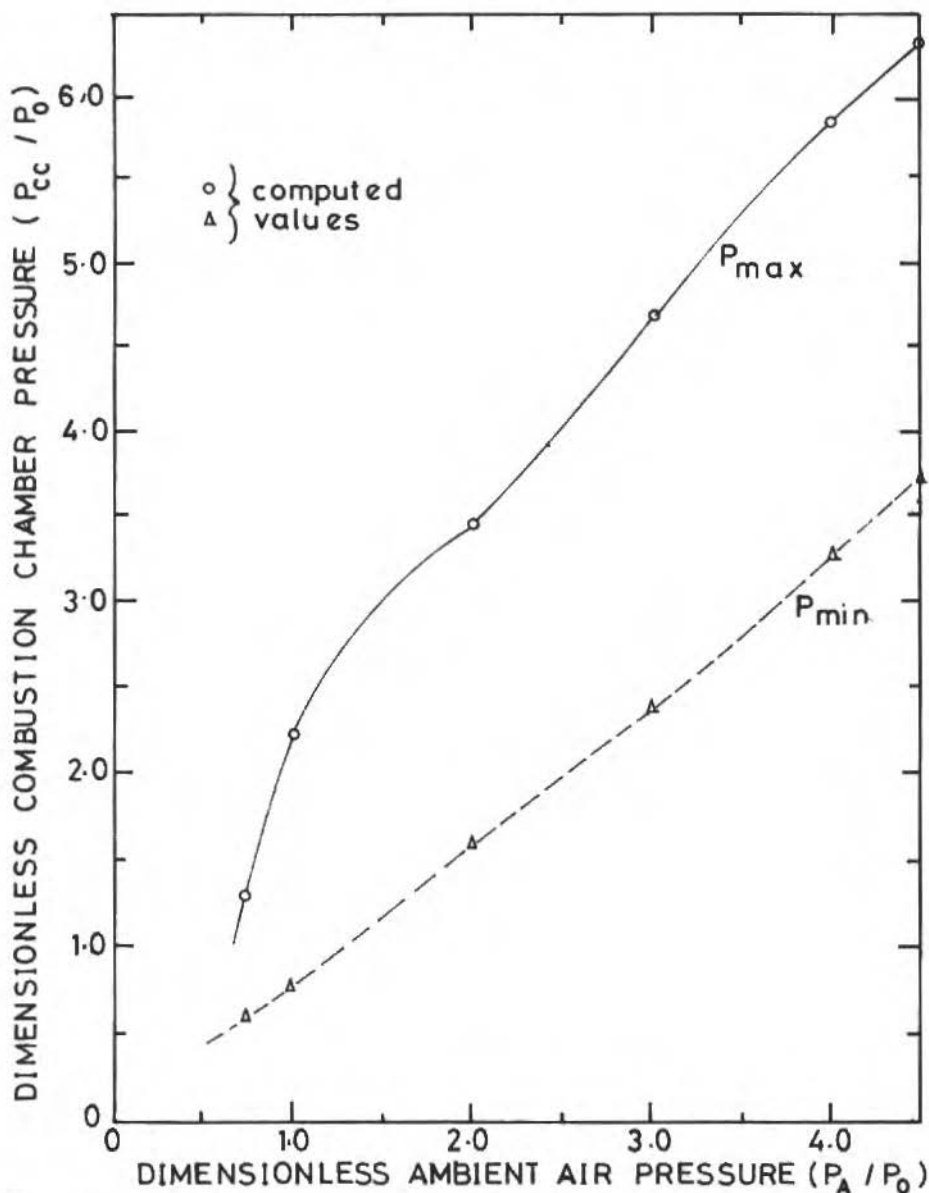
Figure 4. Predicted variation of combustion chamber pressure with ambient air pressure at a fuel flow rate of 7.24 kg/h. The dimensionless ambient temperature was fixed at 1.0.
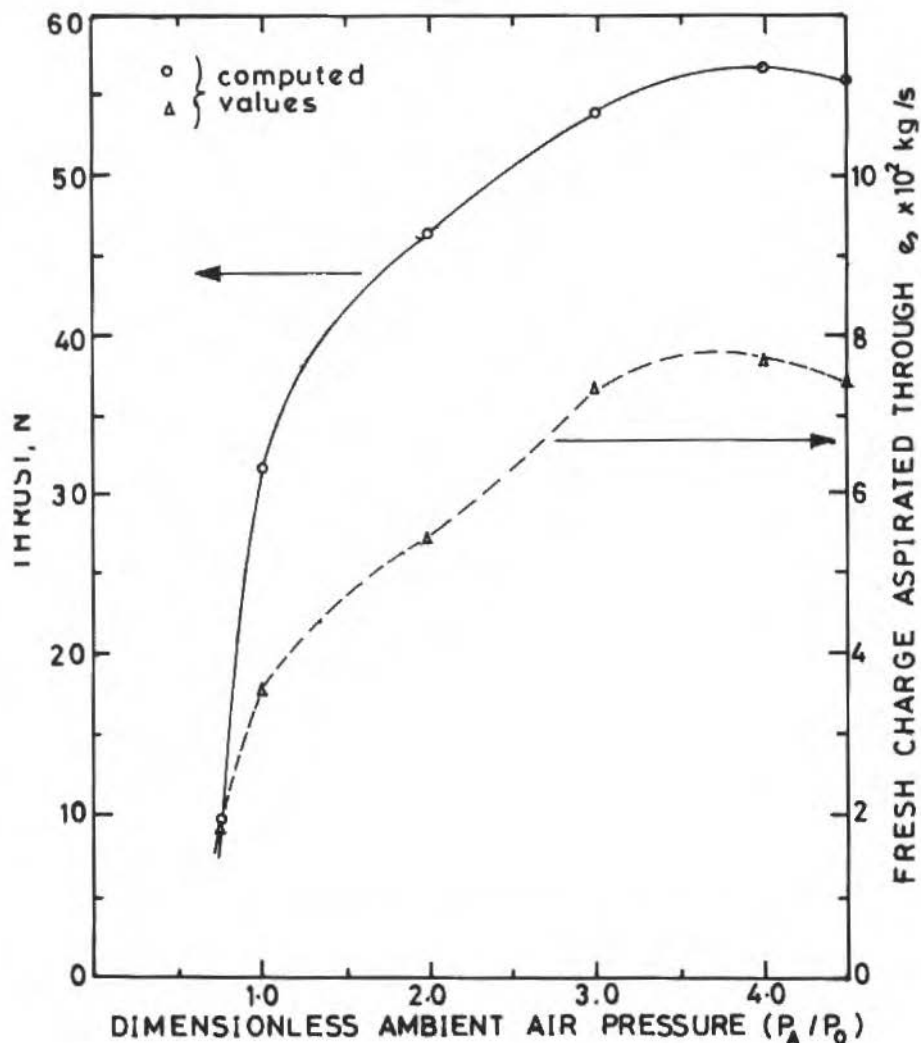
Figure 5. Predicted variation of total thrust generated at e_1 and e_4 and the rate of flow of fresh charge into the combustion chamber through e_2, with ambient pressure, at a fuel flow rate of 7.24 kg/h. The dimensionless ambient temperature was fixed at 1.0.
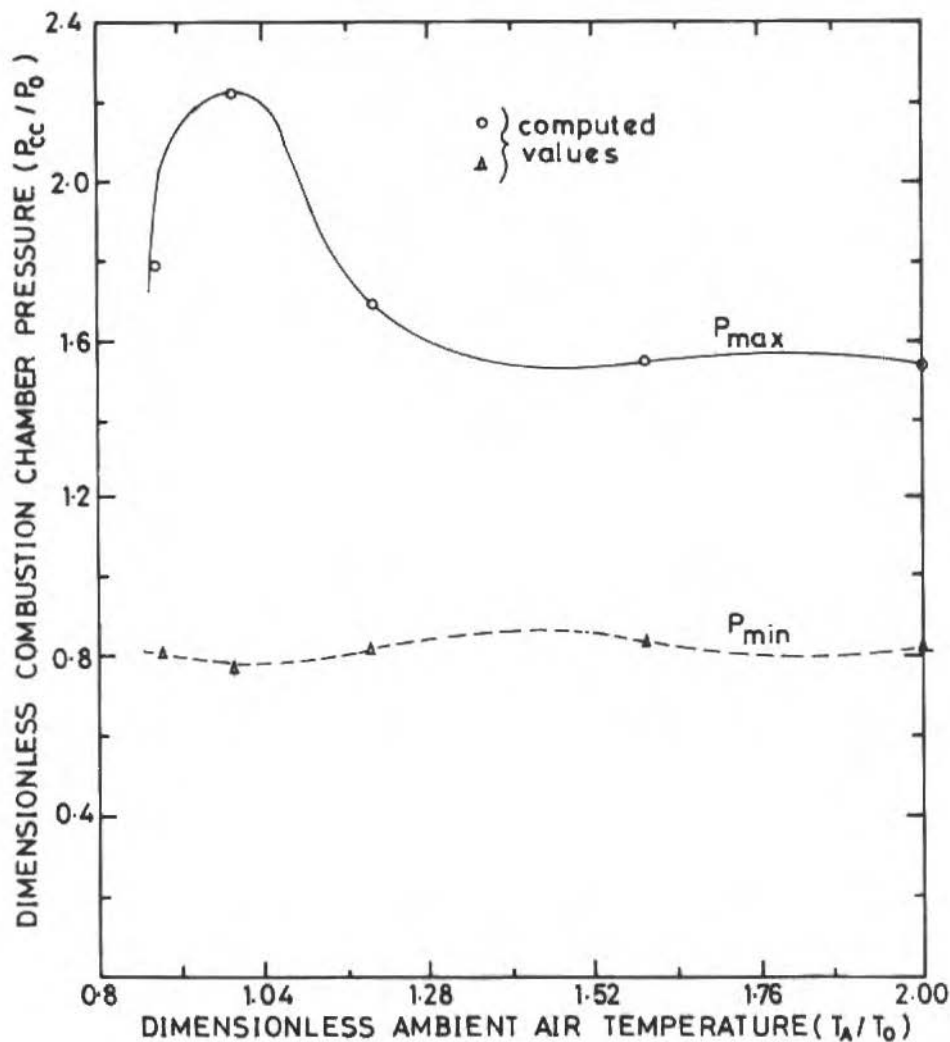
Figure 6. Predicted variation of combustion chamber pressure with ambient air temperature at a fuel flow rate of 7.24 kg/h. The dimensionless ambient pressure was fixed at 1.0.
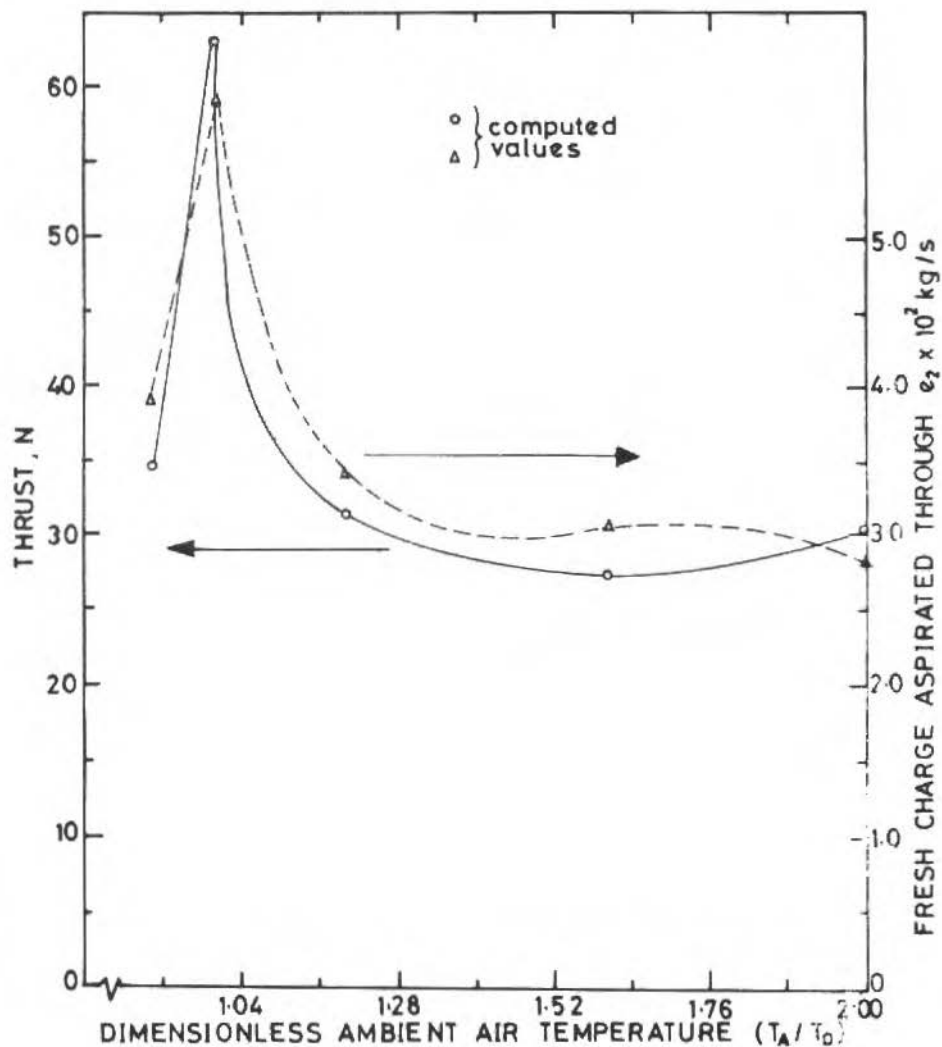
Figure 7. Predicted variation of total thrust generated at e_1 and e_4 and the rate of flow of fresh charge into the combustion chamber through e_2, with ambient air temperature, at a fuel flow rate of 7.24 kg/h. The dimensionless ambient pressure was fixed at 1.0.

This was due to shortage of oxygen in the combustion chamber. This shows that the comubstor with its present geometry, may need to be equipped with a supercharger at the inlet before it works efficiently at high altitudes.

Above an ambient temperature of 1, the pulsation amplitude, total thrust generated at e_1 and e_4, and the rate of flow of fresh charge through e_2 reduced with temperature as shown in Figures 6 and 7. This was largely attributable to the reduction in the density of the fresh charge through e_2 which caused a shortage of oxygen in the combustion chamber.

Poor performance was also observed when the ambient temperature was 0.9 (-13.05^0C) as shown in Figures 6 and 7. To get a good performance under such operating conditions, the pulsed combustor needs to be insulated with suitable materials, or with air, by shrouding it. The pulsed combustor used for de-icing railway track switches by Ringer et al [16] and SWINGFIRE pulsed combustor used to warm up cold-soaked engines by Huber [17] were shrouded.

In the case of shrouded pulsed combustor taking its fresh air from a compressor outlet, the increase of ambient pressure and temperature go together. The performance of the combustor when it was operated in ambient air at a typical compressor output nondimensional pressure and temperature of 4.0 and 1.6 respectively, is shown in the last row of Table VIII. The performance was good but lower than that in ambient air of pressure 4.0 and temperature 1.0. This shows that an optimum performance of valveless pulsed combustors can be expected in gas turbine application, if there is intercooling between the compressor and the pulsed combustor.

Table VIII. Predicted performance of the pulsed combustor with variation of ambient pressure and temperature. The fuel flow rate is 7.24 kg/h and reference pressure and temperature are 88.25 kPa and 289 K respectively.

Ambient Pressure P'_A	Ambient Temperature T'_A	$P'_{max} - P'_{min}$ in combustion chamber	Total thrust generated (N)
1.00	1.00	1.457	31.72
3.00	1.00	2.301	54.00
4.00	1.00	2.548	56.51
1.00	1.00	1.457	31.72
1.00	1.20	0.871	15.71
1.00	1.60	0.727	13.80
4.00	1.60	2.196	46.95

CONCLUSIONS

A mathematical model for optimizing the geometry of pulsed combustors has been presented. The model shows that the alteration of the gas dynamics causing shortage of fresh air in the combustion chamber is what degrades the performance of the pulsed combustor when the geometry employed differs from the optimum one.

Results obtained show that pulsation amplitude in the combustor increases with intake pressure whereas it decreases with intake temperature. In gas turbine application of valveless pulsed combustors, an optimum performance can be expected if there is intercooling between the compressor and the pulsed combustors.

ACKNOWLEDGEMENTS

REFERENCES

[1] BAIRD, M.H.I. Vibrations and Pulsations – Bane or Blessing? British Chem. Engrg., Vol. II, No. 1, pp. 20–25, 1966.

[2] KENTFIELD, J.A.C., REHMAN, A. and CRONJE, J. Performance of Pressure-Gain Combustors without Moving Parts, J. Energy, Vol. 4, No. 2, pp. 56–63, 1980.

[3] HANBY, V.I. Convective Heat Transfer in a Gas-Fired Pulsating Combustor, A.S.M.E. paper No. 68-WA/FU-1.

[4] CORLISS, J.M., PUTNAM, A.A., MURPHY, M.J. and LOCKLIN, D.W. NO_x Emissions from Several Pulse Combustors, A.S.M.E. Paper No. 84-JPGC-APC-2.

[5] KENTFIELD, J.A.C., FERNANDES, L.C.V. Improvements to the Performance of a Prototype Pulse, Pressure Gain, Gas-Turbine Combustor, A.S.M.E. Paper No. 89-GT-277.

[6] SERVANTY, P. Design and Testing of Harmonic Burners for Low Power Gas Turbines, Proceedings of the First International Symposium of Pulsating Combustion, Univ. of Sheffield, 1971.

[7] MARZOUK, E.S. A Theoretical and Experimental Investigational of Pulsed Pressure-Gain Combustion. Ph.D. Thesis, the University of Calgary, Calgary, Canada, 1974.

[8] CRONJE, J.S. An Experimental and Theoretical Study, Including Frictional and Heat Transfer Effects of Pulsed Pressure-Gain Combustion. Ph.D. Thesis, the University of Calgary, Calgary, Canada, 1979.

[9] COURANT, R. and HILBERT, D. Method of Mathematical Physics, Interscience Publishers, John Wiley and Sons, New York, Vol. 2, 1962.

[10] RUDINGER, G. Nonsteady Duct Flow Wave-Diagram Analysis, Dover Publications Inc., New York, 1969.

[11] OLORUNMAIYE, J.A. Numerical Simulation and Experimental Studies of Highly-Loaded Valveless Pulsed Combustors. Ph.D. Thesis, The Univ. of Calgary, Calgary, Canada, 1985.

[12] BENSON, R.S., GARG, R.D. and WOOLLAT, D. A Numerical Solution of Unsteady Flow Problems, Int. J. Mech. Sci., 6, pp. 117–144, 1964.

[13] OLORUNMAIYE, J.A. Computer Programs for the Numerical Simulation of Highly-Loaded Valveless Pulsed Combustors. Report No. 314, Dept. of Mech. Engrg., The Univ. of Calgary, Calgary, Canada, 1984.

[14] OLORUNMAIYE, J.A. and KENTFIELD, J.A.C. Numerical Simulation of Valveless Pulsed Combustors, Acta Astronautica, Vol. 19, No. 8, pp. 669–679, 1989.

[15] PORTER, C.D. Valveless-Gas-Turbine Combustors with Pressure Gain, A.S.M.E. Paper No. 58-GTP-11.

[16] RINGER, T.R., LANE. J.F. and SLAWINSKI, P.P. A Pulsating Combustion System to Protect Railway Track Switches in Snow and Ice Conditions, Proc. First Int. Symposium on Pulsating Combustion, Univ. of Sheffield, 1971.

[17] HUBER, L. Swingfire Operated Heating Unit for Commercial Vehicles, ATZ Technical Review of the Automotive Industry, 66th Year, No. 2, pp. 31–37, 1964.

COMPARISON OF SOME NUMERICAL SCHEMES FOR THE COMPUTATION OF INVISCID FLOWS WITH STRONG DISCONTINUITIES

COMPARAÇÃO ENTRE ALGUNS ESQUEMAS NUMÉRICOS PARA CÁLCULO DE ESCOAMENTOS NÃO-VISCOSOS COM DESCONTINUIDADES FORTES

Marcos A. Ortega
Marco A.M. Carvalho
Instituto Tecnológico de Aeronáutica
Centro Técnico Aeroespacial
12225 São José dos Campos SP, Brasil

João L.F. Azevedo
Instituto de Aeronáutica e Espaço
Centro Técnico Aeroespacial
12225 São José dos Campos SP, Brasil

ABSTRACT

Solutions for the flow in a shock tube of infinite extent are presented for several values of the initial pressure ratio. The physical situation is modelled through the use of the one-dimensional Euler equations and the solution is numerical. Three algorighms are implemented, each representative of a certain class, namely, the centered difference algorithm of Beam and Warming, the flux vector splitting upwind difference algorithm of Steger and Warming and a TVD – Total Variation Diminishing – scheme due to Harten. The main objective of the paper is to compare the performance of these numerical procedures for a non-steady flow with strong discontinuities. Results show that the best performing scheme is the TVD, followed by the flux-split upwind procedure.

Keywords: Numerical Methods ▪ Finite Differences ▪ Centered Operators ▪ Upwind Operators ▪ Flux Vector Splitting ▪ Methods TVD ▪ Shock Tube

RESUMO

Soluções para o escoamento em um tubo de choque de comprimento infinito são apresentadas para vários valores da razão inicial de pressões. A situação física é modelada por meio das equações de Euler e a solução final é numérica. Três algoritmos foram implementados, cada um representativo de uma certa classe, a saber, algoritmo de diferenças centradas de Beam e Warming, algoritmo tipo vetor de fluxo separado de Steger e Warming e algoritmo tipo TVD devido a Harten. O principal objetivo deste trabalho é comparar o desempenho desses esquemas numéricos para um escoamento não-permanente com descontinuidades fortes. Os resultados obtidos mostram que o esquema com melhor desempenho é o método TVD seguido do algoritmo de Steger e Warming.

Palavras-chave: Métodos Numéricos ▪ Diferenças Finitas ▪ Operadores Centrados ▪ Operadores Up-wind ▪ Separação de Vetores de Fluxo ▪ Métodos TVD ▪ Tubo de Choque.

INTRODUCTION

Euler numerical simulation codes, besides several other important character-
istics, have to provide some means for controlling nonlinearities. This must
be so, because the Euler equations constitute an inviscid model and, conse-
quently, as opposed to the Navier-Stokes equations, do not contain any natural
dissipation mechanism that would eliminate high frequencies due to non-linear
effects. In general, there are two ways of handling this problem. Either one
should explicitly introduce artificial dissipation terms to a centered difference
algorithm, or an upwind difference algorithm should be used. Moreover, there
is always the possible drawback of solution oscillations in the passage through
shock waves, which, by the way, is one of the main sources of nonlinearities in
the flowfield.

A typical example of a centered difference scheme is the well-known Beam
and Warming algorithm [1], [2]. This algorithm, to which artificial dissipation
terms of linear and non-linear nature have been systematically aggregated, has
been successfully applied to a wide variety of problems (see, for example, [3],
[4], [5] and [6]). Another notable example is the work of Jameson et al. [7],
where the time integration is performed through the use of an explicit Runge-
Kutta procedure. In contrast to these, another class of schemes can be found in
the literature, under such names as monotone, flux split, flux difference, total
variation diminishing (TVD), that employs some form of upwind differencing.
Representatives of this category are the works of Steger and Warmining [8],
Harten [9], Osher and Chakravarthy [10], van Leer [11], and Roe [12].

The main objective of this paper is the implementation of a number of
algorithms belonging to both classes in order to test and confront their
abilities in terms of overall accuracy, stability, computer costs, and discontinuity
capturing and resolution. This, we hope, will permit the reader a quick
assessment of the several techniques employed and also provide some hints
for the proper selection of one of those schemes. The flow in a shock tube of
infinite extent is selected as the test case. The reason for this choice rests on the
fact that this flow contains different types of discontinuites, such as shock and
expansion waves as well as contact surfaces. As one of the primary interests
of this research is to investigate the behavior of the solution in the crossing of
discontinuities, the shock tube is a natural choice. Mathematically, the flow

in a shock tube of infinite extent can be recognized as a Riemann problem. Details of this flow are described in standard gasdynamic texts [13].

The algorithms selected for the solution of the shock tube are: the Beam and Warming algorithm with non-linear artificial dissipation, the Steger and Warming flux vector splitting scheme, and Harten's TVD method. The work to be reported herein is organized in the following way. Initially, the Euler equations and the essentials of the several algorithms are introduced. After this, results are presented and discussed.

THE EULER EQUATIONS

Consider a long tube in which two masses of gas with different static pressures are initially at rest and separated by a diaphragm. The diaphragm is suddenly burst, and then an expansion wave propagates into the high-pressure chamber, while a shock wave, followed by a contact discontinuity, propagates into the low-pressure chamber. With the exception of the thin boundary layer that grows from behind the wave fronts, the flow in the tube is essentially one-dimensional. The modelling of the gas as an inviscid fluid makes the geometry of the problem perfectly one-dimensional. In view of this, the developments that follow will consider only one space coordinate. It should be borne in mind, however, that most of the theory here treated is straightforwardly extended to two and three dimensions.

The one-dimensional Euler equations in strong conservation-law form can be written as

$$\frac{\partial Q}{\partial t} + \frac{\partial E}{\partial x} = 0 \, , \tag{1}$$

where

$$Q = \begin{bmatrix} \rho \\ \rho u \\ e \end{bmatrix} \qquad E = \begin{bmatrix} \rho u \\ \rho u^2 + p \\ (e + p) \, u \end{bmatrix} \tag{2}$$

Here ρ is the density, u is the velocity, and p is the pressure. The total energy per unit volume, e, is related to the specific internal energy, e_i, by

$$e = \rho \left(e_i + \frac{u^2}{2} \right) \tag{3}$$

The fluid is considered to be a perfect gas and, then, the equation of state is

$$p = (\gamma - 1)\, \rho\, e_i \, , \tag{4}$$

where $\gamma = c_p/c_v$. The specific heats, c_p and c_v, are taken as constants.

THE ALGORITHMS

The Beam and Warming Algorithm

Linear Dissipation

The structure of the Beam and Warming algorithm, as implemented in this work, is based on the implicit time-marching Euler scheme, which can be written as

$$Q^{n+1} = Q^n + \Delta t \left(\frac{\partial Q}{\partial t}\right)^{n+1} + \Delta t \mathcal{O}(\Delta t) \, . \tag{5}$$

The objective now is to write the algorithm in the so called delta form. To this end, we substitute Eq.(1) in the above equation. After this, the algebraic steps are: (i) linearization of the flux vector E by means of a simple Taylor expansion and (ii) introduction of centered differences to approximate the spatial derivatives. The delta form is finally obtained as

$$(I + \Delta t\, \delta_x A^n)\, \Delta_t Q^n = -\Delta t(\delta_x E^n) \, , \tag{6}$$

where $\Delta_t Q^n = \Delta Q^n = (Q^{n+1} - Q^n)$, $A = (\partial E/\partial Q)$ is the flux Jacobian matrix and δ_x is a centered difference operator. The algorithm represented by Eq.(6) is first order accurate in time and second order accurate in space.

In order to maintain the numerical stability of the scheme represented by Eq.(6), we have to introduce artificial dissipation terms. Hence, we rewrite this equation as

$$(I + \Delta t\, \delta_x A^n + D_I)\, \Delta_t Q^n = -\Delta t(\delta_x E^n) + D_E \, , \tag{7}$$

where

$$D_I = -\varepsilon_I\, \Delta t(\nabla_x \Delta_x) \tag{8}$$

is the implicit second-difference dissipation, and D_E is the explicit artificial dissipation term. In its simplest form, this term would be given by a fourth-difference formula as

$$D_E = -\varepsilon_E \Delta t (\nabla_x \Delta_x)^2 .\tag{9}$$

Here, ε_I and ε_E are constant (linear) coefficients that control the amount of added artificial dissipation. The Δ_x and ∇_x are standard, first order, forward and backward difference operators, respectively.

As can be realized, a fourth-order term was added to the right side of the basic algorithm to control nonlinear instabilities. Ideally, in order to balance the algorithm, a fourth-difference term should also be added to the left side. However, this would imply the inversion of a sparse pentadiagonal block matrix, and this is too expensive. For the sake of cost-effectiveness, a second-difference implicit dissipation is added to stabilize the implicit term. It is important to observe that these added terms modify the original partial differential equations and the coefficients used should be kept as small as possible while still maintaining stability. As a starting point the parameter ε_E can be chosen to be $\mathcal{O}(1)$ and $\varepsilon_I = 2\varepsilon_E$ (see [14]). The dissipation terms are scaled with Δt in order to guarantee steady state solutions independent of the time step.

Nonlinear Dissipation

In smooth regions of the flowfield, the scheme represented by Eq.(7) is sufficiently strong to control oscillations that might appear. On the other hand, when faced with strong discontinuities, as for example shock waves, severe oscillations can occur. These localized instabilities can be traced to the problem of differencing across the discontinuity, where too big of a differencing stencil is employed. In order to avoid this drawback, Jameson et al. [7] have introduced the idea of switching between a fourth-difference dissipation term, which gives rise to a five point differencing stencil, to a second-order term whenever the pressure gradient becomes too strong. This is the essence of the non-linear artificial dissipation scheme. Pulliam [14] has adapted Jameson's model to the present notation and the following expression results:

$$D_E = \nabla_x (\sigma_{i+1} + \sigma_i)(\varepsilon_i^{(2)} \Delta_x Q_i - \varepsilon_i^{(4)} \Delta_x \nabla_x \Delta_x Q_i)\tag{10}$$

where

$$\varepsilon_i^{(2)} = k_2 \Delta t \max(\Upsilon_{i+1}, \ \Upsilon_i, \ \Upsilon_{i-1}) \ ,$$
$$\varepsilon_i^{(4)} = \max(0, \ k_4 \Delta t - \varepsilon_i^{(2)}) \ .$$

Typical values of the constants are $k_2 = 1/4$ and $k_4 = 1/100$ and the maximum function is used to spread the second-difference dissipation range over a few grid points. Values of Υ_i are given by

$$\Upsilon_i = \frac{|p_{i+1} - 2p_i + p_{i-1}|}{|p_{i+1} + 2p_i + p_{i-1}|} \ .$$

The term σ_i is a spectral radius scaling defined by

$$\sigma_i = u + a \ ,$$

where a is the local speed of sound.

By observing Eq. (10), one can understand the logic of the scheme. The first term of this equation is a second-difference dissipation with an extra pressure gradient coefficient to increase its value near shocks. Besides enhancing the role of the second-difference term, the coefficient $\varepsilon_i^{(2)}$ also acts through $\varepsilon_i^{(4)}$ until the fourth-difference dissipation is switched off. This happens when the pressure gradient is such that the second-difference nonlinear coefficient is larger than the constant fourth-difference coefficient. This occurs near shocks or in regions of steep pressure variations as, for example, at the nose region of an airfoil.

The Flux Splitting Scheme of Steger and Warming

Numerical schemes for the solution of the unsteady inviscid gasdynamic equations can be based on approximating spatial derivatives through the use of centered or one-sided difference operators. In subsonic regions, however, only centered difference operators lead to numerical methods that are simultaneously stable for both the positive and negative characteristic speeds [8]. Notwithstanding this, several stable upwind methods have been developed and are in wide use today. The stabilizing technique that each of these methods aggregates corresponds to some form of flux splitting.

Several reasons justify the use of one-sided difference operators. For an implicit algorithm, the one we have implemented, there is a definite gain in efficiency,

because the scheme can lead to sparse lower, or upper, **triangular banded** matrices, that are more easily inverted than the tridiagonal and pentadiagonal matrices usually associated with centered methods. In this item we present the main features of the flux splitting idea together with the principal points of the Steger and Warming algorithm.

Flux Splitting

By using Eq. (2) the flux Jacobian matrix $A = (\partial E / \partial Q)$ can be easily obtained,

$$A = \begin{bmatrix} 0 & 1 & 0 \\ \frac{1}{2}(\gamma - 3)\,u^2 & (3 - \gamma)\,u & (\gamma - 1) \\ (\gamma - 1)\,u^3 - \frac{\gamma e u}{\rho} & \gamma\frac{e}{\rho} - \frac{3}{2}(\gamma - 1)\,u^2 & \gamma u \end{bmatrix} \qquad (11)$$

The characteristic speeds, i.e., eigenvalues, of A are

$$\lambda_1 = u, \qquad \lambda_2 = u + a, \qquad \lambda_3 = u - a . \qquad (12)$$

In subsonic regions $|u| < a$, and the eigenvalues are of mixed sign since $u + a$ and $u - a$ are of opposite sign.

Suppose, for now, that the flux vector E can be split into two parts as

$$E = E^+ + E^- \qquad (13)$$

such that the subvector E^+ is associated with the positive eigenvalues of A and E^- is associated with the negative eigenvalues. Substituting the relation above in Eq.(1) there results

$$\frac{\partial Q}{\partial t} + \frac{\partial E^+}{\partial x} + \frac{\partial E^-}{\partial x} = 0 , \qquad (14)$$

what would allow the use of a backward difference operator to approximate $(\partial E^+ / \partial x)$ and a forward operator to approximate $(\partial E^- / \partial x)$. By virtue of these one-sided approximations we are, in fact, respecting the directions of characteristic signal propagation.

The question to be posed now is: How can the flux vector E be, effectively, split? To answer this question one has to rely on two fundamental properties.

The first corresponds to the fact that the flux Jacobian matrix A has a complete set of real eigenvalues. The second concerns the structure of the inviscid gas-dynamic equations in conservation-law form. These equations have the remarkable property that if the equation of state has the functional form

$$p = \rho f(c_i) \,, \tag{15}$$

then the nonlinear flux vector $E(Q)$ is a homogeneous function of degree one in Q. This means that $E(\alpha Q) = \alpha E(Q)$ for any value of α. By simply inspecting the equation of state, Eq.(4), one can see that it has the form of (15), what guarantees that $E(Q)$ is a homogeneous function of degree one. Hence, it is easy to show that

$$E = AQ \,. \tag{16}$$

The basis, then, for splitting vector E are the two properties mentioned above ([15], [16]). Let us proceed and derive the split form of E to be used in the next item.

The starting point is the fact that there is a similarity transformation for the matrix A [8], such that

$$T^{-1} A T = \Lambda \,, \tag{17}$$

where, for the inviscid gasdynamic equations, $T = MX$, $T^{-1} = X^{-1}M^{-1}$ and Λ is a diagonal matrix whose diagonal terms are the eigenvalues of A. Matrices M and X and their inverses for one and two space dimensions are given in Ref. [15] and for three space dimensions in [17]. From Eq. (17) we obtain

$$A = TT^{-1}ATT^{-1} = T\Lambda T^{-1} \,, \tag{18}$$

which, substituted in Eq. (16), gives

$$E = AQ = T\Lambda T^{-1} Q \,. \tag{19}$$

Any eigenvalue λ_i can be written as

$$\lambda_i = \lambda_i^+ + \lambda_i^- \,, \tag{20}$$

where

$$\lambda_i^+ = \frac{\lambda_i + |\lambda_i|}{2} \,, \qquad \lambda_i^- = \frac{\lambda_i - |\lambda_i|}{2} \,. \tag{21}$$

Observe that if $\lambda_i \geq 0$, then $\lambda_i^+ = \lambda_i$, $\lambda_i^- = 0$, with the converse result for $\lambda_i < 0$. Considering the above expressions, it is possible to split the diagonal matrix

$$\Lambda = \Lambda^+ + \Lambda^- , \tag{22}$$

where Λ^+ and Λ^- have as diagonal elements λ_i^+ and λ_i^-, respectively. Substituting Eq. (22) in Eq. (19) one obtains

$$E = T(\Lambda^+ + \Lambda^-) T^{-1}Q = (A^+ + A^-) Q = E^+ + E^- , \tag{23}$$

where

$$A^+ = T\Lambda^+ T^{-1}, \quad A^- = T\Lambda^- T^{-1}, \quad E^+ = A^+ Q, \quad E^- = A^- Q , \tag{24}$$

and

$$A = A^+ + A^- . \tag{25}$$

The eigenvalues of A, given by Eq. (12), are then split, according to Eqs. (20) and (21), into

$$\begin{aligned}
\lambda_1^+ &= \frac{u + |u|}{2} , & \lambda_1^- &= \frac{u - |u|}{2} , \\
\lambda_2^+ &= \frac{u + a + |u + a|}{2} , & \lambda_2^- &= \frac{u + a - |u + a|}{2} , \\
\lambda_3^+ &= \frac{u - a + |u - a|}{2} , & \lambda_3^- &= \frac{u - a - |u - a|}{2}
\end{aligned} \tag{26}$$

The subvectors E^+ and E^-, for the case when $0 \leq u \leq a$, are given by

$$E^+ = \frac{\rho}{2\gamma} \begin{bmatrix} 2\gamma u + a - u \\ 2(\gamma - 1)u^2 + (u + a)^2 \\ (\gamma - 1)u^3 + \frac{1}{2}(u + a)^3 + \frac{(3-\gamma)(u+a)a^2}{2(\gamma-1)} \end{bmatrix} , \tag{27}$$

$$E^- = \frac{\rho}{2\gamma} \begin{bmatrix} u - a \\ (u - a)^2 \\ \frac{(u-a)^3}{2} + \frac{(3-\gamma)(u-a)a^2}{2(\gamma-1)} \end{bmatrix} \tag{28}$$

If $u > a$, the subvectors are simply

$$E^+ = E , \qquad E^- = 0 , \tag{29}$$

where vector E is given in Eq. (2).

Finally, it is important to observe that the eigenvalue splitting represented by Eq. (26) is not unique and other splittings into positive and negative parts are possible (see, for details [8]).

The Algorithm of Steger and Warming

Without approximating spatial derivatives by difference operators, Eq.(6) can be rewritten as

$$\left(I + \Delta t \, \frac{\partial A^n}{\partial x}\right) \Delta_t Q^n = -\Delta t \left(\frac{\partial E^n}{\partial x}\right) . \tag{30}$$

Introducing Eqs. (23) and (25) into the expression above, the following relation is obtained

$$\left[I + \Delta t \left(\frac{\partial A^+}{\partial x} + \frac{\partial A^-}{\partial x}\right)\right] \Delta_t Q^n = -\Delta t \left(\frac{\partial E^+}{\partial x} + \frac{\partial E^-}{\partial x}\right) . \tag{31}$$

Approximating, now, spatial derivatives by one-sided, first-order, difference operators, there results

$$[I + \Delta t(\nabla_x A^+ + \Delta_x A^-)] \Delta_t Q^n = -\Delta t(\nabla_x E^+ + \Delta_x E^-) . \tag{32}$$

The final form of the algorithm can be established by profitting from the approximate factorization idea due to Beam and Warming [2]. One finally obtains

$$[I + \Delta t(\nabla_x A^+)][I + \Delta t(\Delta_x A^-)] \Delta_t Q^n = -\Delta t(\nabla_x E^+ + \Delta_x E^-) . \tag{33}$$

As the reader can readily observe, this scheme involves the inversion of only triangular banded matrices and, consequently, tridiagonal matrices are avoided.

A linear analysis would easily show that, in this case, no error is introduced by the approximate factorization. The spatial accuracy of the scheme proposed can be improved, without impairing efficiency – specially for steady state problems

- if we use second-order, one-sided difference operators in the right hand side of the algorithm.

TVD – Total Variation Diminishing Scheme

The Concept of Total Variation Diminishing Algorithms

In general, methods based on centered difference approximations do not behave well in the calculation of flowfields with strong discontinuities, because even seemingly small oscillations can be disastrous in these cases. The reasons for this have been already discussed above. When facing this kind of difficulty, upwind schemes have proven to be much more robust. However, upwind strategies lose, in what concerns code simplicity and computational efficiency. For example, the formation, in every cycle, of matrices A^+ and A^-, and vectors E^+ and E^-, is very expensive. Furthermore, upwind methods have a different drawback – they possess numerically stable, nonphysical expansion shocks [10].

A new class of methods, known as TVD – Total Variation Diminishing – schemes, has, recently, called the attention of many authors, due to its robustness and its remarkable capability of reproducing strong discontinuities with great accuracy and resolution, even for extreme high Mach numbers. Other authors argue, however, that TDV schemes are complicated and that the development of (mainly) implicit algorithms for more complex flowfield situations is a very difficult task [14].

The basic idea underlying TVD schemes is not exactly new; it rests upon the pioneering work of Godunov [18]. Considering that the TVD theory is really much involved, there is no room, in a paper of this nature, to present it. We refer the reader, then, to the pertinent literature (for example, Refs. [9] and [10]). Next, we will try, however, to give the general idea of the fundamental concepts involved in a total variation diminishing scheme. Let us represent by Q_i^n the numerical approximation to the solution of Eq.(1) at grid point i and at time $n\Delta t$. We define the total variation of the solution as

$$TV(Q) = \sum_{i=-\infty}^{\infty} |Q_{i+1} - Q_i| \, . \tag{34}$$

In our notation, the general form of a the TVD algorithm is

$$Q_i^{n+1} = Q_i^n - \frac{\Delta t}{\Delta x} \left(\widetilde{E}_{i+\frac{1}{2}}^m - \widetilde{E}_{i-\frac{1}{2}}^m \right) ,$$ (35)

where, typically, the numerical flux function has the following generic form:

$$\widetilde{E}_{i+\frac{1}{2}} = \widetilde{E}(Q_{i-k+1}, \dots, Q_{i+k}) = \frac{1}{2} \left[E(Q_i) + E(Q_{i+1}) - \int_{Q_i}^{Q_{i+1}} \mathcal{F}(Q) \, dQ \right] .$$ (36)

In the above expression, $\mathcal{F}(Q)$ is some function of the vector of conserved variables. If $m = n$ the method is explicit, otherwise, if $m = n + 1$ it is implicit.

A finite-difference numerical method such as given by Eq. (35) is said to be total variation diminishing – TVD – (sometimes also called total variation nonincreasing – TVNI) if, for every solution Q^n, which has a limited total variation, it is possible to write

$$TV(Q^{n+1}) \le TV(Q^n) .$$ (37)

The Method of Harten

We consider now the 5-point, second order accurate, explicit TVD scheme of Harten [9]. The basic form of the algorithm when applied to general systems of conservation laws can be written as

$$Q_i^{n+1} = Q_i^n - \lambda_h (\bar{E}_{i+\frac{1}{2}} - \bar{E}_{i-\frac{1}{2}}) ,$$ (38)

where $\lambda_h = (\Delta t / \Delta x)$ and

$$\bar{E}_{i+\frac{1}{2}} = \frac{1}{2} \left\{ E_i^n + E_{i+1}^n \right.$$

$$\left. + \frac{1}{\lambda_h} \sum_{k=1}^{3} R_{i+\frac{1}{2}}^k \left[g_i^k + g_{i+1}^k - F_h^k (\nu_{i+\frac{1}{2}}^k + \gamma_{i+\frac{1}{2}}^k) \, \alpha_{i+\frac{1}{2}}^k \right] \right\} .$$ (39)

It is important to observe that, in these expressions, vectors Q and E are still given by Eq.(2). We describe below the several new parameters appearing in Eq. (39).

Function F_h^k

In this scheme, this function corresponds to the artificial dissipation. It is given by

$$F_h^k(y) = \begin{cases} \frac{y^2}{4\varepsilon} + \varepsilon , & \text{for } |y| < 2\varepsilon , \\ |y| , & \text{for } |y| \geq 2\varepsilon . \end{cases} \tag{40}$$

Harten suggests the usage of $\varepsilon = 0.1$ for genuinely nonlinear fields (shock and expansion waves) and $\varepsilon = 0$ for linearly degenerated fields (contact discontinuities). The symbol y in the formulas above is a dummy variable.

Argument of Function F_h^k

The argument of F_h^k is given by the sum

$$\nu_{i+\frac{1}{2}}^k + \gamma_{i+\frac{1}{2}}^k . \tag{41}$$

The first term, $\nu_{i+\frac{1}{2}}^k$, has the form

$$\nu_{i+\frac{1}{2}}^k = \lambda_h \lambda_a^k (v_{i+\frac{1}{2}}) , \tag{42}$$

where λ_a^k are the eigenvalues of the problem

$$\begin{aligned} \lambda_a^1 &= u - a , \\ \lambda_a^2 &= u , \\ \lambda_a^3 &= u + a , \end{aligned} \tag{43}$$

and $v_{i+\frac{1}{2}}$ is an average of vector Q in the interval i and $i+1$. Harten suggests a simple arithmetic average, i.e.,

$$v_{i+\frac{1}{2}} = Q_{i+\frac{1}{2}} = \frac{1}{2} \left(Q_i + Q_{i+1} \right) . \tag{44}$$

In spite of Harten's suggestion we have implemented Roe's averaging scheme (see [9]). Having determined this average, other quantities can be calculated at the position $(i + \frac{1}{2})$. For example,

$$\hat{u} = u_{i+\frac{1}{2}} = \frac{(\rho u)_{i+\frac{1}{2}}}{\rho_{i+\frac{1}{2}}} . \tag{45}$$

The second term in Eq. (41) is written as

$$\gamma_{i+\frac{1}{2}}^{k} = \begin{cases} \frac{(g_{i+1}^{k}+g_{i}^{k})}{\alpha_{i+\frac{1}{2}}^{k}} , & \text{when } \alpha_{i+\frac{1}{2}}^{k} \neq 0 , \\ 0 , & \text{when } \alpha_{i+\frac{1}{2}}^{k} = 0 . \end{cases} \tag{46}$$

Values for the parameter $\alpha_{i+\frac{1}{2}}^{k}$ will be given below.

Function g_i^k

The expression for function g_i^k is

$$g_i^k = s_{i+\frac{1}{2}}^{k} \max \left[0, \min \left(|\tilde{g}_{i+\frac{1}{2}}^{k}|, \ s_{i+\frac{1}{2}}^{k} \ \tilde{g}_{i-\frac{1}{2}}^{k} \right) \right] ,$$
$$s_{i+\frac{1}{2}}^{k} = sign(\tilde{g}_{i+\frac{1}{2}}^{k}) , \tag{47}$$
$$\tilde{g}_{i+\frac{1}{2}}^{k} = \frac{1}{2} \left[F_h^k(\nu_{i+\frac{1}{2}}^{k}) - (\nu_{i+\frac{1}{2}}^{k})^2 \right] (\alpha_{i+\frac{1}{2}}) .$$

Values of $R_{i+\frac{1}{2}}^{k}$ and $\alpha_{i+\frac{1}{2}}^{k}$

The symbol R^k stands for the eigenvectors to the right of Jacobian matrix A. They are

$$R^1(Q) = \begin{bmatrix} 1 \\ u - a \\ H - ua \end{bmatrix} , \quad R^2(Q) = \begin{bmatrix} 1 \\ u \\ \frac{1}{2} u^2 \end{bmatrix} , \quad R^3(Q) = \begin{bmatrix} 1 \\ u + a \\ H + ua \end{bmatrix} , \tag{48}$$

where $H = (e + p)/\rho$ is the total enthalpy.

Values of α^k are given by

$$\alpha^1 = \frac{1}{2}(c_1 - c_2) , \quad \alpha^2 = [\rho] - c_1 , \quad \alpha^3 = \frac{1}{2}(c_1 + c_2) , \tag{49}$$

where

$$c_1 = (\gamma - 1) \frac{[e] + \frac{1}{2} \hat{u}^2 [\rho] + \hat{u}[\rho u]}{\hat{a}^2} ,$$
$$c_2 = \frac{[\rho u] - \hat{u}[\rho]}{\hat{a}} . \tag{59}$$

The symbol [ ] indicates a jump variation, i.e., for any property b,

$$[b] = b_R - b_L = (b_{i+1} - b_i) .\tag{51}$$

On the other hand, $\hat{u}$ and $\hat{a}$ stand for average values of velocity and local speed of sound, respectively. These averages are referred to the state defined by Eq.(44), or its corresponding with Roe's averaging procedure, and Eq.(45).

Initially, the algorithm, as defined by the equations above, was implemented, and the parameter ε was given the value 0.1. However, there was a severe loss of resolution at the contact surface. The reason for this solution behavior is most certainly due to this value of ε, which introduces an amount of artificial dissipation that is excessive for a linearly degenerated field. In order to circumvent this situation, a modification was introduced in the function g_i^k (see, for details, Ref. [9], p. 377). Resolution was, then, completely recovered.

RESULTS AND DISCUSSION

The flow development in the shock tube was obtained for several values of the ratio p_4/p_1, where subscripts 4 and 1 indicate properties at the high and at the low pressure chambers, respectively, before the rupture of the diaphragm. In all cases we have made $T_1 = T_4$, just as a matter of convenience.

In all the figures presented in this work, dashed lines correspond to the analytical solution, whereas solid lines and/or symbols represent the present numerical solutions. Figs. 1 to 12 illustrate the relative performance of the three algorithms implemented. Figs. 1 to 6 refer to the case $(p_4/p_1) = 5$, and Figs. 7 to 12 refer to the $(p_4/p_1) = 20$ case. The TVD algorithm of Harten is the one that gives the best performance, both in terms of accuracy as well as resolution. The upwind scheme of Steger and Warming presents good accuracy, but lacks in resolution, while the nonlinear artificial dissipation algorithm of Beam and Warming does not perform well, especially for high pressure ratios.

It is important to observe that the upwind scheme maintains good accuracy, even in the case $(p_4/p_1) = 20$, but there is oscillation, an overshoot before the contact surface and an undershoot before the shock wave. Both upwind and centered algorithms do not give good resolution at the crossing of the contact discontinuity. This is to be expected, because these schemes do not

aggregate a special numerical mechanism to handle this kind of situation. On the contrary, the method of Harten, as we have mentioned above, is prepared to deal with such form of discontinuity. In order to gain in resolution at the contact surface, we are, at present, incorporating to the nonlinear artificial dissipation algorithm, an additive procedure which relies on the value of the temperature gradient.

However, perhaps even more disturbing than the oscillations at shocks or contact discontinuities is the inability of the centered scheme to capture the correct shock speed. This is quite evident from Figs. 1 and 7. Moreover, Fig. 9 seems to indicate that the speed of the contact discontinuity is not being correctly captured by the centered scheme either. This type of behavior is typically associated with non-conservative schemes, which is not the case here. At the moment, these observations are still being further investigated, but there is some expectation that this behavior could be traced to the use of rather different artificial dissipation models on the left- and right-hand sides of the present implementation of the Beam and Warming algorithm.
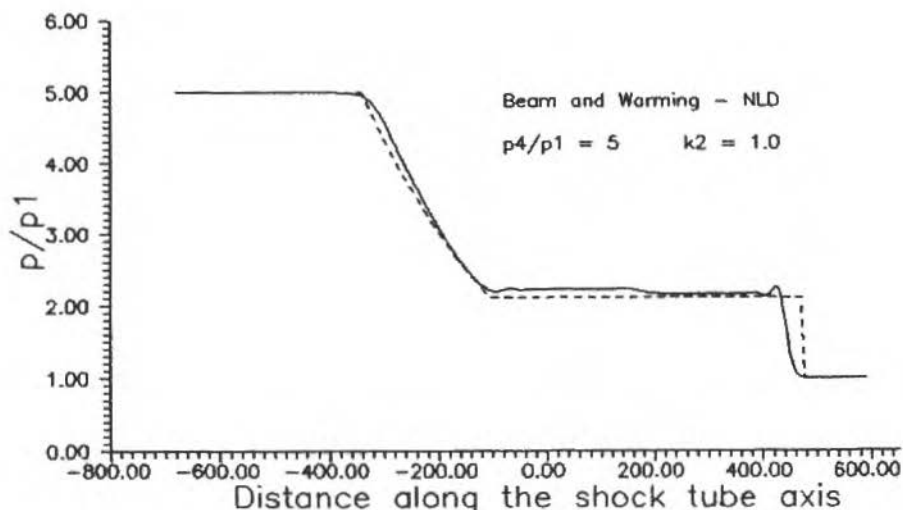
Figure 1. Pressure distribution after $t = 1$ s for the Beam and Warming scheme.
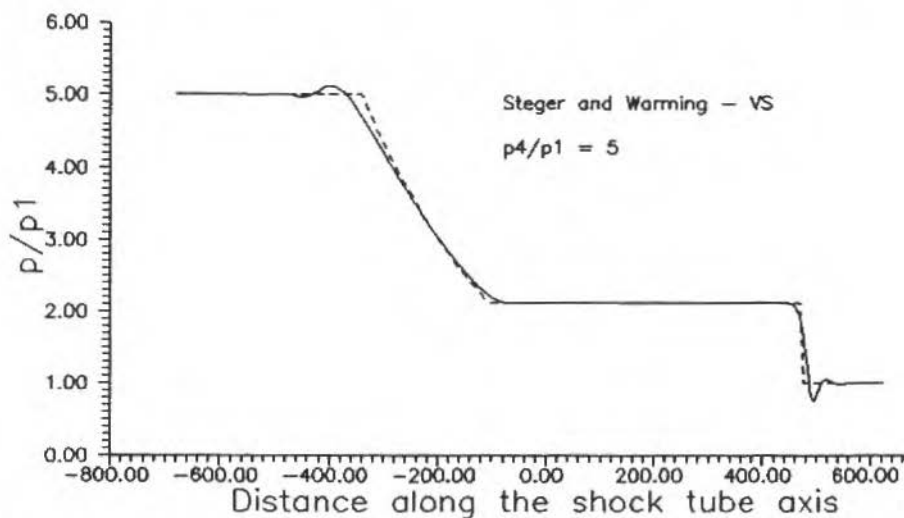
Figure 2. Pressure distribution after $t = 1$ s for the Steger and Warming scheme.
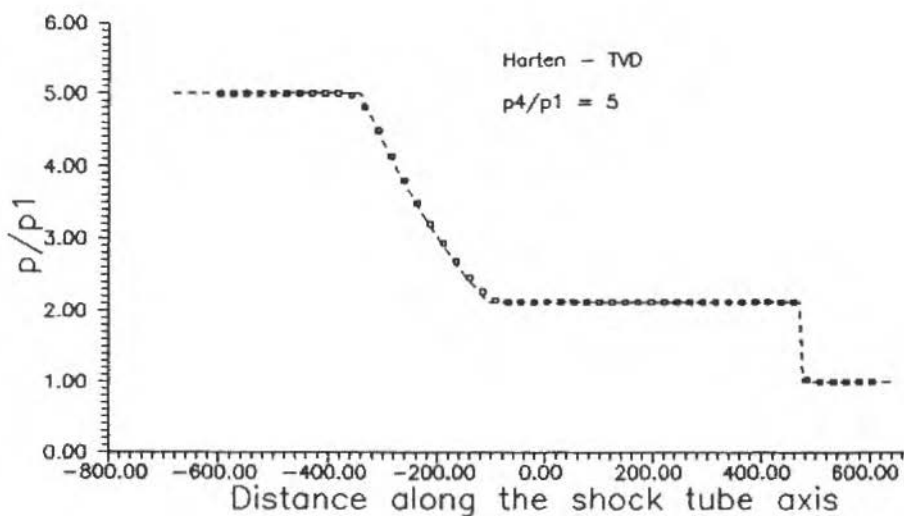
Figure 3. Pressure distribution after $t = 1$ s for the TVD scheme.

M.A. Ortega, M.A.M. Carvalho and J.L.F. Azevedo
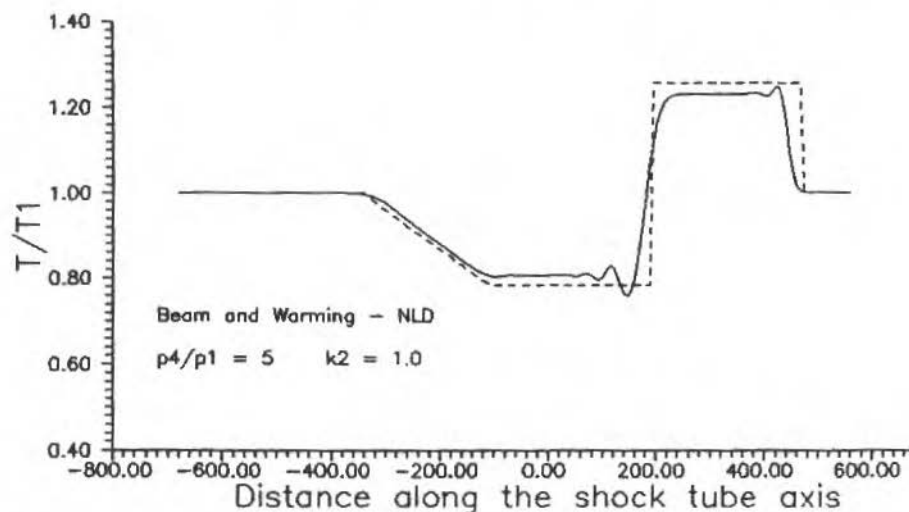
Figure 4. Temperature distribution after $t = 1$ s for the Beam and Warming scheme.
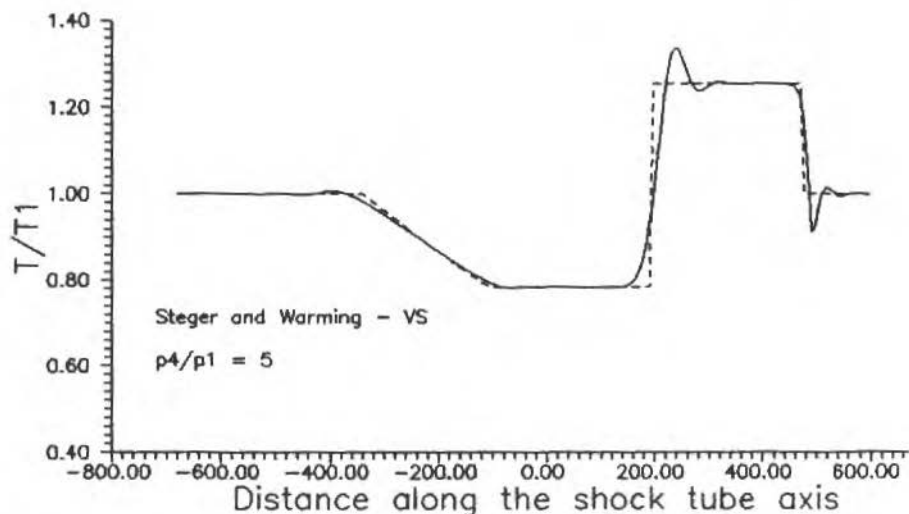
Figure 5. Temperature distribution after $t = 1$ s for the Steger and Warming scheme.
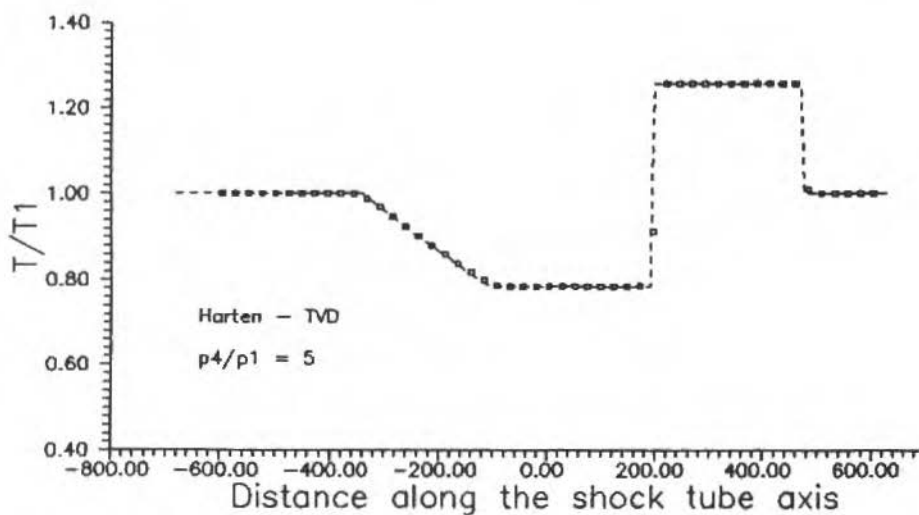
Figure 6. Temperature distribution after $t = 1$ s for the TVD scheme.
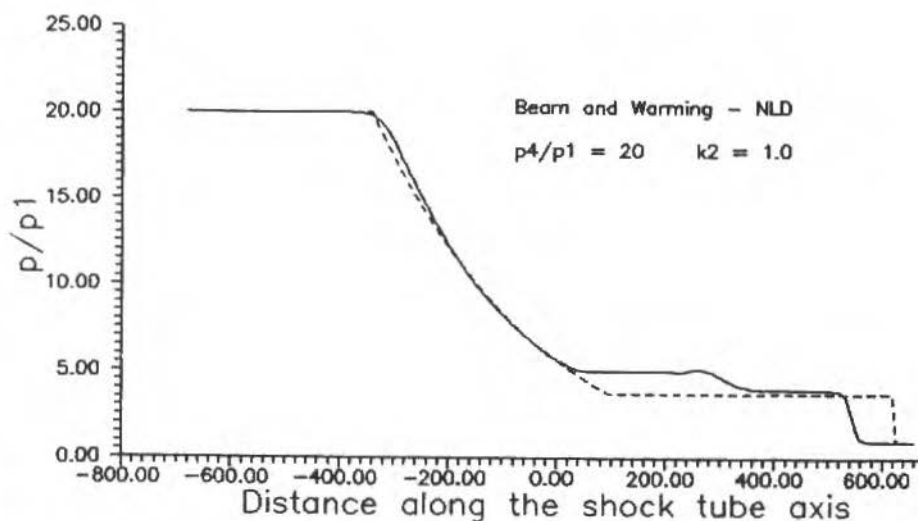
Figure 7. Pressure distribution after $t = 1$ s for the Beam and Warming scheme.
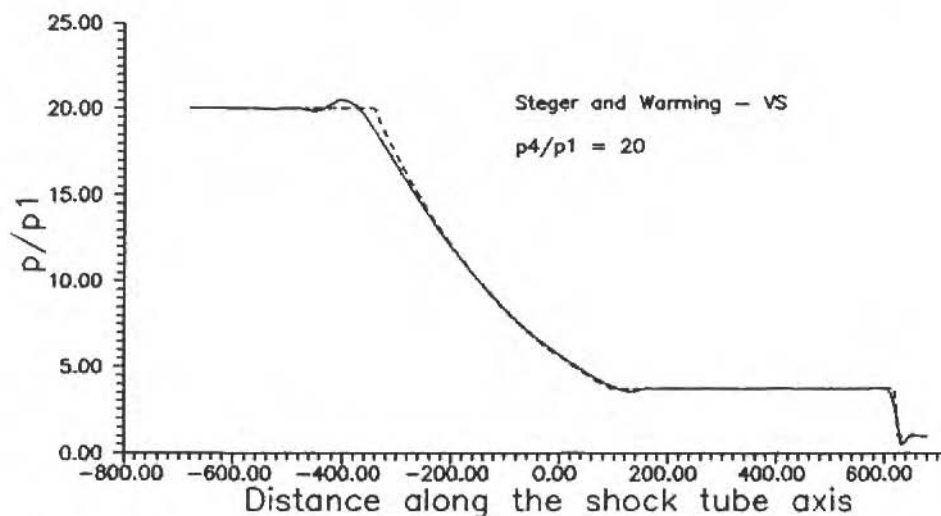
Figure 8. Pressure distribution after $t = 1$ s for the Steger and Warming scheme.
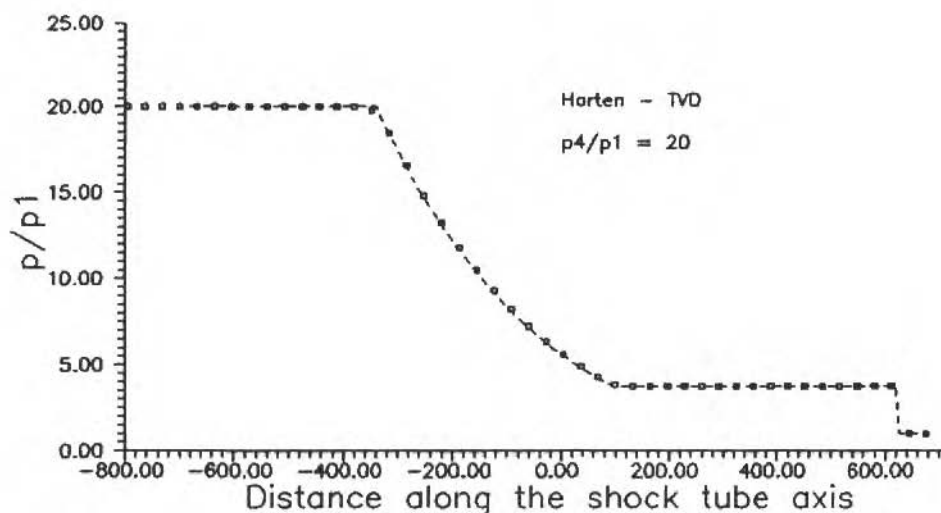
Figure 9. Pressure distribution after $t = 1$ s for the TVD scheme.
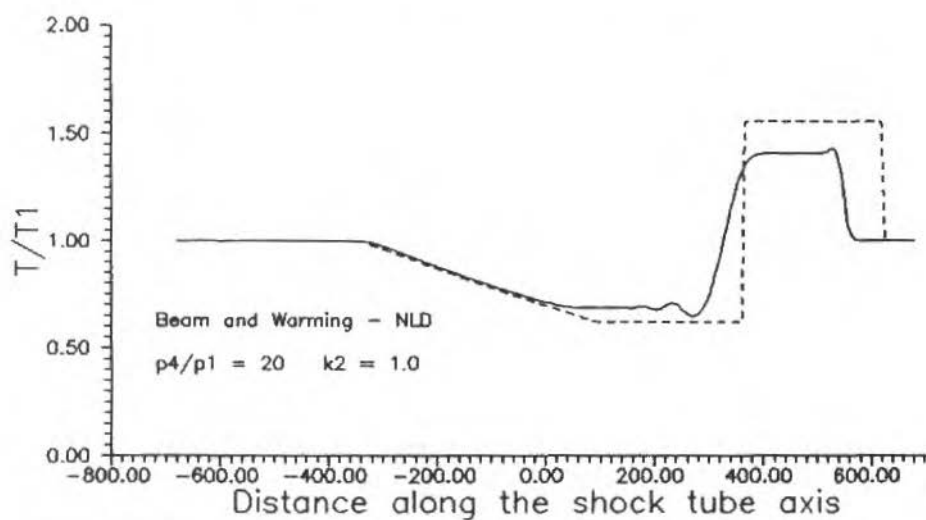
Figure 10. Temperature distribution at $t = 1$ s for the Beam and Warming scheme.
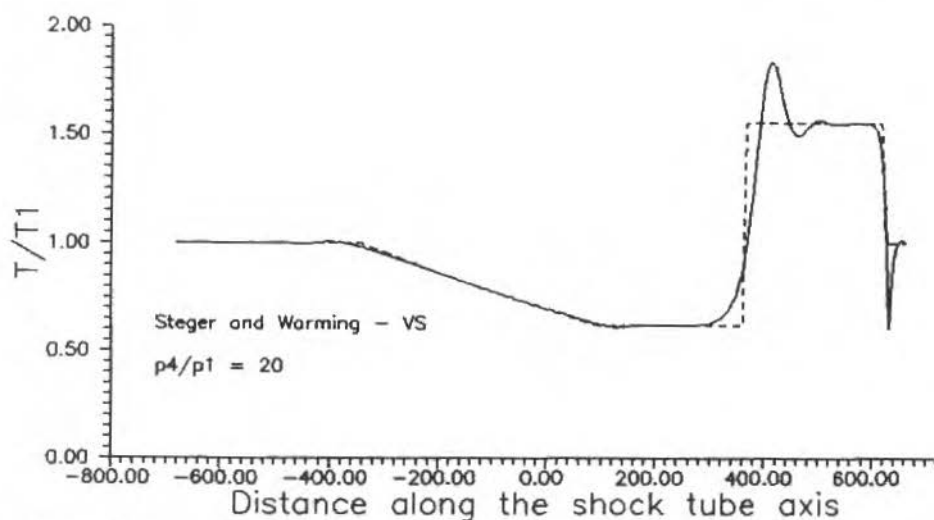
Figure 11. Temperature distribution at $t = 1$ s for the Steger and Warming scheme.
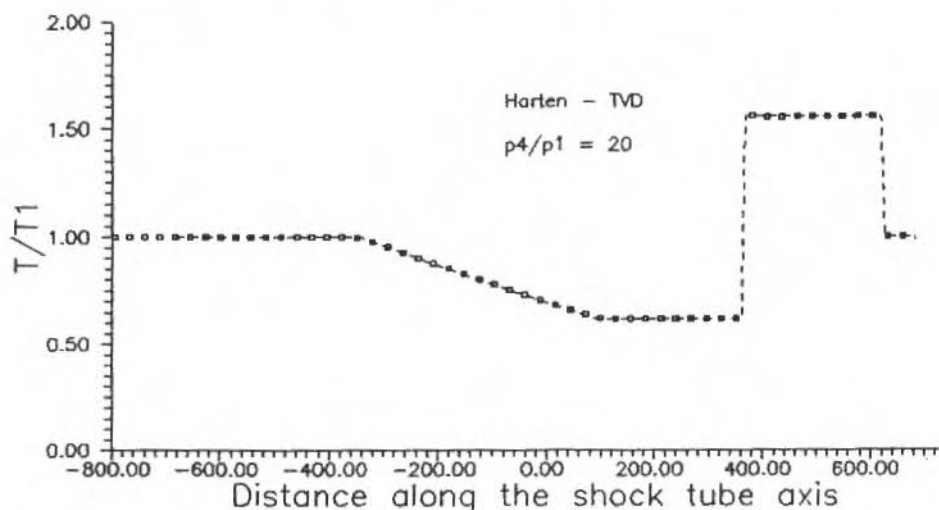
Figure 12. Temperature distribution at $t = 1$ s for the TVD scheme.

In Figs. 13 and 14 one can see the Beam and Warming algorithm solution for $(p_4/p_1) = 1.56$ and $k_2 = 0.25$. For the cases reported in Figs. 1, 4, 7 and 10, we have used $k_2 = 1.0$ in order to avoid large oscillations at the shock. The idea now is to test the behavior of the algorithm in the transonic range – the shock wave Mach number is 1.1. As can be observed, there is good accuracy and resolution, but, unexpectedly, there appeared large oscillations at the tail of the expansion wave. We have also run the Beam and Warming algorithm for $(p_4/p_1) = 5$ and $k_2 = 0.25$ in order to assess the influence of the amount of artificial dissipation. These results are shown in Figs. 15 and 16. The code ran stably and, in fact, there were no major differences to the case $k_2 = 1.0$ (see Figs. 1 and 4).

Finally, Figs. 17 and 18 show the solution of the shock tube problem for $(p_4/p_1) = 50$. This is a rather severe test problem and, as can be seen from these figures, the performance of the TVD scheme of Harten is outstanding. It must be observed, however, that the scheme of Harten is designed for the kind of physical situation that was treated in this work. This explains, at least in part, the good performance of the method.
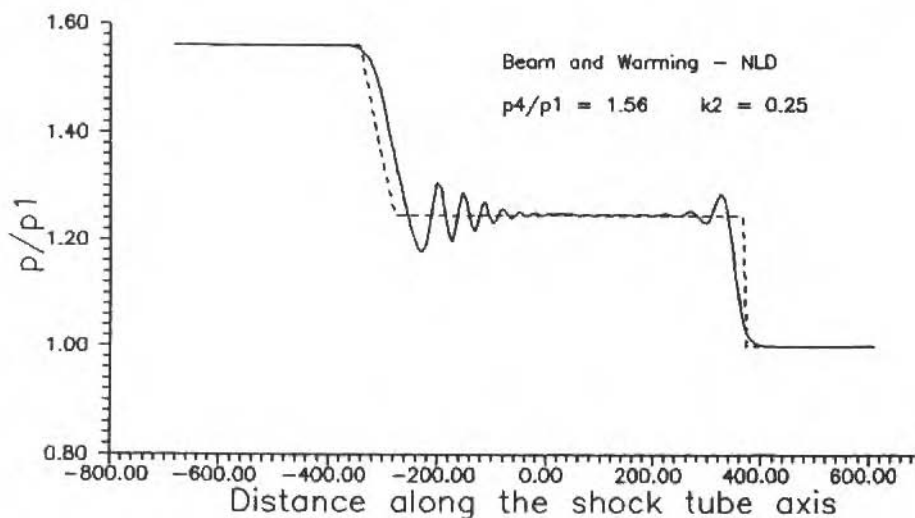
Figure 13. Results for centered algorithm with small pressure ratio ($t = 1$ s).
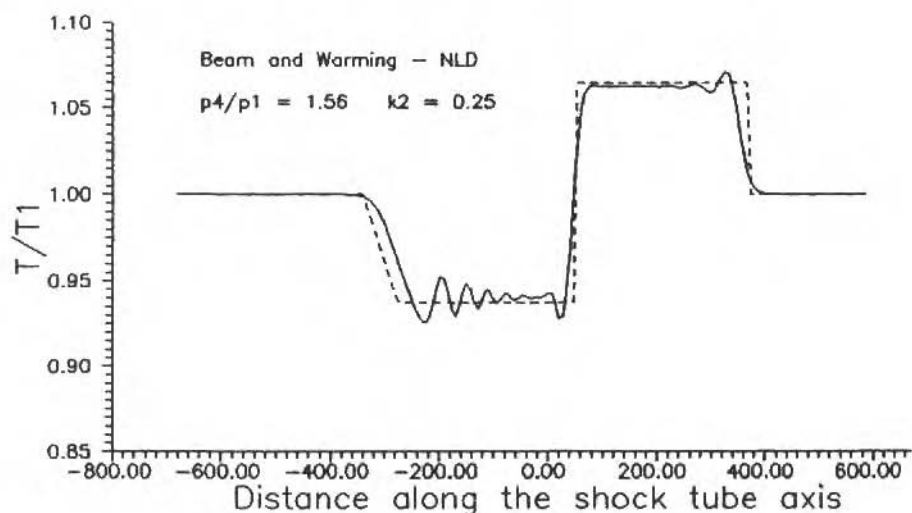
Figure 14. Results for centered algorithm with small pressure ratio ($t = 1$ s).
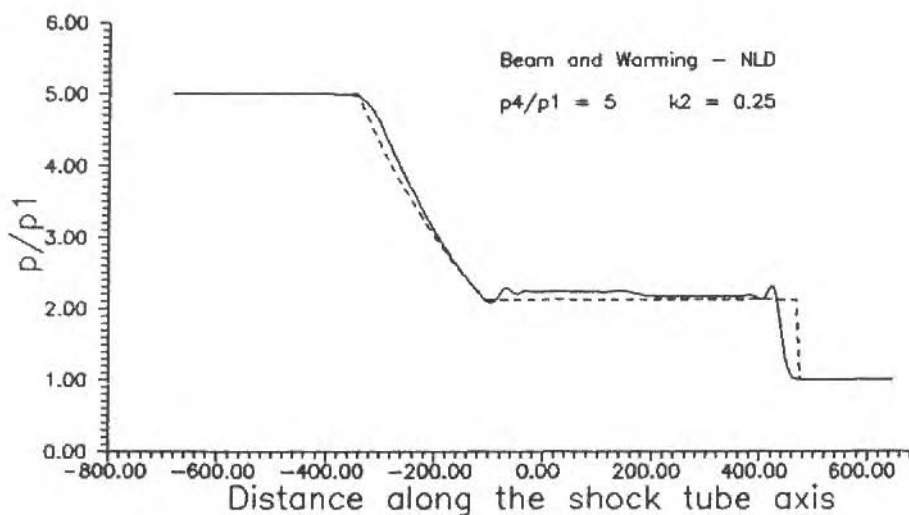
Figure 15. Effect of explicit artificial dissipation term on the pressure ($t = 1$ s).
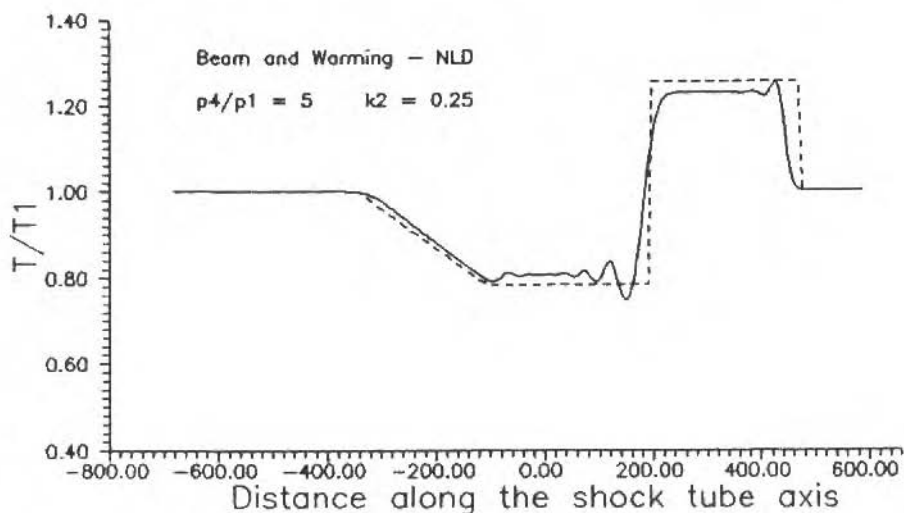
Figure 16. Effect of explicit artificial dissipation term on the temperature ($t = 1$ s).
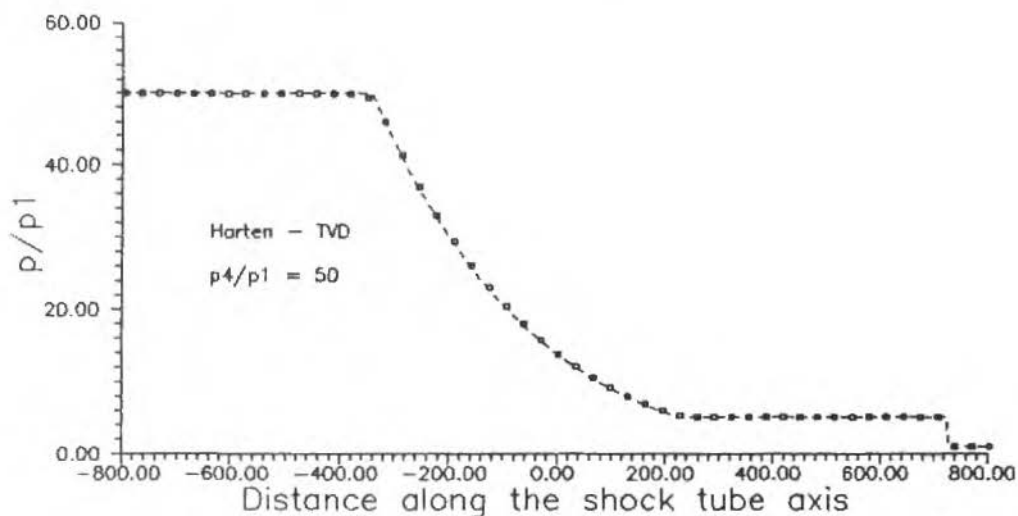
Figure 17. Behavior of TVD scheme for very high pressure ratio ($t = 1$ s).
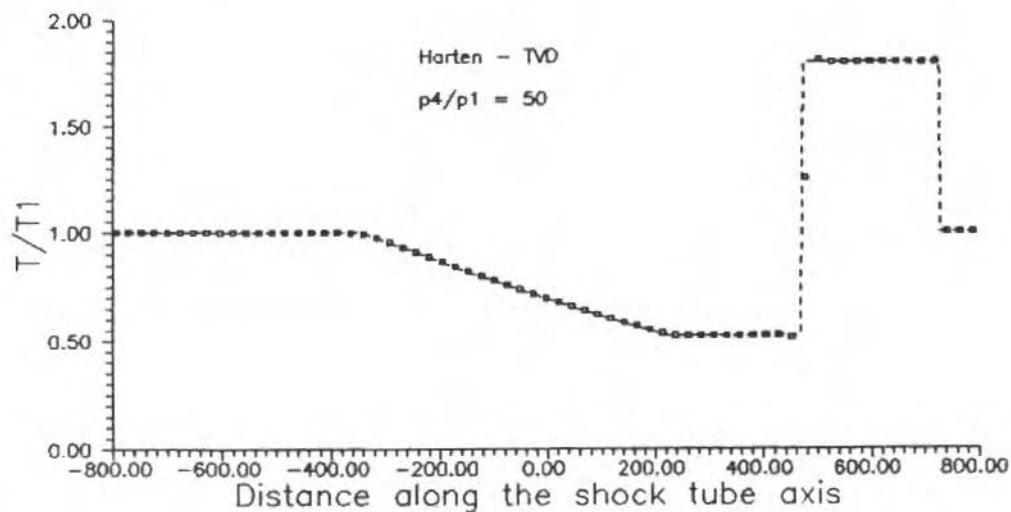
Figure 18. Behavior of TVD scheme for very high pressure ratio ($t = 1$ s).

The codes were run in an IBM-like PS-386/33 microcomputer and the computation times per cycle were 1.3 s, 2.3 s and 1.8 s, respectively, for the TVD, flux-split upwind and centered difference schemes. In each case the numerical grid consisted of 200 equally spaced points. The reader should keep in mind, however, that the TVD scheme involves much more operations per time step than the other two schemes. The reason why the computational times reported above seem to favor the TVD scheme is that we are comparing an explicit TVD algorithm with two implicit schemes. Hence, this is actually not a fair comparison of computational efficiency. Explicit versions of the centered and flux-split upwind schemes would certainly run much faster than the TVD scheme.

CONCLUDING REMARKS

The wave system development in a shock tube of infinite extent, which corresponds to a one-dimensional, unsteady flow, was modeled through the use of the Euler equations and solved numerically by means of the Beam and Warming algorithm with nonlinear artificial dissipation, the Steger and Warming flux-split upwind scheme, and Harten's TVD method. A systematic comparison has shown that the best suited numerical technique for the physical situation considered here is a TVD algorithm. This conclusion can certainly be extended to other problems involving strong discontinuities. In spite of some oscillations, the flux-split upwind scheme behaved also quite well, maintaining accuracy even for high values of the initial pressure ratio. This was not the case for the centered difference algorithm, which performed well only for low values of the pressure ratio.

Nevertheless, it is important to remind that the flow in a shock tube is a very specific example of movement in a fluid, in the sense that it is a simple geometry, or configuration, while the physics involved can represent a very severe test case for numerical methods. In general, fluid flow problems of great interest, especially in aerodynamics, are steady, and the bodies involved have complicated two and three dimensional geometries. In these cases, algorithms based on centered differences, or those based on flux vector splitting techniques and one-sided differences, have also shown excellent performance. In terms of the underlying mathematical theory, there is no guarantee that TVD-like schemes will remain TVD, or monotone, in multidimensions. Moreover, the

implementation of implicit TVD formulations typically renders schemes which are not necessarily TVD for the transient portion of the solution. The results here obtained, however, indicate that TVD schemes can be a very good option in any case in which strong shocks, or strong discontinuities in general, are present.

REFERENCES

[1] BEAM, R.M. and WARMING, R.F. An Implicit Finite-Difference Algorithm for Hyperbolic Systems in Conservation-Law Form, Journal of Computational Physics, Vol. 22, Sept. 1976, pp. 87–110.

[2] BEAM, R.M. and WARMING, R.F. An Implicit Factored Scheme for the Compressible Navier-Stokes Equations, AIAA Journal, Vol. 16, No. 4, April 1978, pp. 393–402.

[3] PULLIAM, T.H. and STEGER, J.L. Implicit Finite-Difference Simulations of Three Dimensional Compressible Flow, AIAA Journal, Vol. 18, No. 2, Feb. 1980, pp. 159–167.

[4] PULLIAM, T.H. and STEGER, J.L. Recent Improvements in Efficiency, Accuracy and Convergence for Implicit Approximate Factorization Algorithms, AIAA Paper 85-0360, AIAA 23rd Aerospace Sciences Meeting, Reno, Nevada, Jan. 1985.

[5] PULLIAM, T.H. Euler and Thin Layer Navier-Stokes Codes: ARC2D, ARC3D, Notes for Computational Fluid Dynamics User's Workshop, The University of Tennessee Space Institute, Tullahoma, Tenn., March 12-16, 1984.

[6] PULLIAM, T.H. Implicit Finite-Difference Methods for the Euler Equations, in Advances in Computational Transonics, W.G. Habashi, editor, Pineridge Press, Swansea, U.K., 1985, pp. 503–542.

[7] JAMESON, A., SCHMIDT, W. and TURKEL, E. Numerical Solutions of the Euler Equations by Finite Volume Methods Using Runge-Kutta Time-Stepping Schemes, AIAA Paper 81-1259, 1981.

[8] STEGER, J.L. and WARMING, R.F. Flux Vector Splitting of the Inviscid Gas Dynamic Equations with Applications to Finite-Difference Methods, Journal of Computational Physics, Vol. 40, 1981, pp. 263-293.

[9] HARTEN, A. High Resolution Schemes for Hyperbolic Conservation Laws, Journal of Computational Physics, Vol. 49, 1983, pp. 357–393.

[10] OSHER, S. and CHAKRAVARTHY, S. Upwind Schemes and Boundary Conditions with Applications to Euler Equations in General Geometries, Journal of Computational Physics, Vol. 50, 1983, pp. 447–481.

[11] VAN LEER, B. Flux-Vector Splitting for the Euler Equations, Eighth International Conference on Numerical Methods in Fluid Dynamics, Springer Lecture Notes in Physics No. 170, edited by E. Krause, 1983.

[12] ROE, P.L. Characteristic-Based Schemes for the Euler Equations, Annual Review of Fluid Mechanics, Vol. 18, 1986, pp. 337-365.

[13] LIEPMANN, H.W. and ROSHKO, A. Elements of Gasdynamics, John Wiley, New York, 1957.

[14] PULLIAM, T.H. Artificial Dissipation Models for the Euler Equations, AIAA Journal, Vol. 24, No. 12, Dec. 1986, pp. 1931-1940.

[15] WARMING, R.F. and BEAM, R.M. On the Construction and Application of Implicit Factored Schemes for Conservation Laws, Symposium on Computational Fluid Dynamics, New York, April 16–17, 1977, SIAM-AMS Proc. 11, 1978, 85.

[16] STEGER, J.L. Coefficient Matrices for Implicit Finite Difference Solution of the Inviscid Fluid Conservation Law Equations, Computer Methods in Applied Mechanics and Engineering, Vol. 13, 1978, pp. 175–188.

[17] WARMING, R.F., BEAM, R.M. and HYETT, B.J. Diagonalization and Simultaneous Symmetrization of the Gas-Dynamic Matrices, Math. Comp., Vol. 29, No. 132, Oct. 1975, pp. 1037–1045.

[18] GODUNOV, S.K. A Finite Difference Method for the Numerical Computation of Discontinuous Solutions of the Equations of Fluid Dynamics, Math. Sb. 47, 1959, pp. 357-393.

Announcement and Call for Papers

FIRST ISHMT-ASME HEAT AND MASS TRANSFER CONFERENCE
(12th NATIONAL HEAT AND MASS TRANSFER CONFERENCE)
Bombay, India, January 5–7, 1994

Heat and mass transfer play a very important role in all industrial process. Hence, a proper understanding of these phenomena is very essential for optimal design of the equipment and components, and efficient operation of various process and industrial plants, ensuring economy and safety. The Indian Society for Heat and Mass Transfer (SHMT) has been acting as a nodal agency in India in stimulating research workers engaged in various areas of heat and mass transfer and bringing them together for fruitful interaction and exchange of views. The ISHMT organized the first National Heat and Mass Transfer Conference at the Indian Institute of Technology, Madras in 1971 and subsequently the conference has been held once every two years all over the country. In all these conferences, many experts from abroad have participated, exchanged technical information and shared their expertise with Indian researchers. With the passing of two decades, the organization has matured. In order to accelerate already existing scientific cooperation between USA and Indian researchers through several cooperative research projects and minimize duplication of research efforts, it has been decided to organize the next national conference as a joint ISHMT-ASME Heat and Mass Transfer Conference as agreed by both societies. Hopefully, this joint conference will encourage broader international participation from other countries for further scientific cooperation.

The aim of the conference is to bring together the researchers and practitioners from India, USA, and other countries to enable discussions and exchange of information in the relevant areas. The major thrust of the conference will be to:
- review the state-of-art
- presentation of new fundamental and applied research results
- identification of possible areas of cooperation between industry and research institutions both in India as well as other countries for mutual benefit.

Contributed papers are solicited in all areas of heat and mass transfer dealing with theory, analysis, experimental work, computational studies, modeling, simulation, design, applications and technology. In addition, there will be keynote addresses and a few state-of-the-art invited lectures by eminent experts, covering up-to-date research and developments in heat and mass transfer areas. There will also be mini-symposia on some specialized subjects, and panel discussions on some of the most important areas of current interest. It is also planned to devote a session for Industry/Research Worker interaction to identify research areas of immediate interest to Industry. There will also be an exhibition of heat and mass transfer equipment. Short courses on the subjects of the most important technological area will also be offered.

Deadlines

- 31 October 1992   Three copies of abstracts due
- 31 December 1992   Notification of abstract acceptance
- 31 March 1993   Full length manuscript due
- 30 June 1993   Notification of paper acceptance
- 31 August 1993   Author-prepared mats due

All papers will go through a strict peer review process. All accepted papers will be published in the hard cover conference proceedings available at the Conference. The Conference language will be English and all papers must be in English. For further information and abstract contact:

- Dr. V. Venkat Raj, Conference Co-Chairman, Reactor Safety Division, Bhabha Atomic Research Centre, Engineering Hall 7, Bombay 400 085, India. Tel. 91-22-555-0847; Fax: 91-22-556-0750.

- Dr. R.K. Shah, Conference Co-Chairman, Harrison Division, GMC, Lockport, NY 14094-1896, USA. Tel.: 1-716-439-3020; Fax: 1-716-439-3648.

- Dr. V.M.K. Sastri, ISHMT Secretary, Department of Mechanical Engineering, Indian Institute of Technology, Madras 600 036, India. Tel.: 91-44-235-1365, Ext. 3694; Fax: 91-44-235-0509.

AN ALGORITHM FOR SIMULATING THE ENERGY TRANSFER PROCESS IN A MOVING SOLID-FLUID MIXTURE

UM ALGORITMO PARA A SIMULAÇÃO DO PROCESSO DE TRANSFERÊNCIA DE ENERGIA EM UMA MISTURA BINÁRIA SÓLIDO-FLUIDO EM MOVIMENTO

Maria Laura Martins Costa
Rubens Sampaio
Department of Mechanical Engineering
Pontifícia Universidade Católica – RJ
Rua Marquês de São Vicente,225
22453 – Rio de Janeiro – Brazil

Rogério Martins Saldanha da Gama
Laboratório Nacional de Computação Científica (LNCC/CNPq)
Rua Lauro Müller,455
22290 – Rio de Janeiro – Brazil

ABSTRACT

In the present work an algorithm for a local simulation of the energy transfer phenomenon in a binary (solid-fluid) moving saturated mixture is proposed. An iterative procedure is used to simulate (employing a Finite Difference approach) the heat transfer in a saturated flow (through a porous medium) between two parallel isothermal plates in which the fluid constituent inlet temperature is the only boundary condition prescribed on x-direction. An exhaustive number of tests have shown that the mentioned procedure (which is independent from initial estimates for both constituent second order partial derivatives on x-direction) consists of an effective way to perform this simulation.

RESUMO

Neste trabalho propõe-se um algoritmo para a simulação local do fenômeno de transferência de energia numa mistura binária (sólido-fluido) saturada em movimento. A transferência de calor num escoamento saturado através de um meio poroso, limitado por duas placas planas paralelas isotérmicas, foi simulada por um processo iterativo usando-se uma abordagem de diferenças finitas. O processo iterativo permite que sejam obtidas aproximações numéricas para a solução do problema prescrevendo-se uma única condição de contorno na direção do escoamento (x): a temperaura de entrada do constituinte fluido. Um número exaustivo de casos testados mostrou que o procedimento mencionado (que independe das estimativas iniciais das derivadas parciais de segunda ordem na direção x para os dois constituintes) é eficiente para a simulação em questão.

NOMENCLATURE

c_i	i-th specific heat
H	channel width
K	specific permeability
k_i	i-th thermal condutivity
L	channel length
q_i	i-th constituent partial heat flux
R	positive factor related to energy generation function
T_i	i-th constituent temperature
$\mathbf{v_F}$	fluid constituent velocity (vector field)
v_F	x-component of fluid constituent velocity
h	heat transfer coefficient
λ	parameter depending on porous matrix
Λ	parameter related to mixture structure
ρ_i	i-th constituent density
φ	porosity
ψ_i	i-th constituent energy generation function

Subscripts

F	fluid constituent
S	solid constituent

Superscripts

l	global iteraction
k	Gauss-Seidel iteraction

INTRODUCTION

The interest on flow through porous media taking into account heat and/or mass transfer is growing significantly nowdays. Interactions between fluids and solids are present in many industrial processes. These fluids may be passed over packed beds of solid material so that a large ratio of surface area to volume is obtained and phenomena such as heat and mass transfer and chemical reactions may occur. The main purpose of this work is to present a procedure which, despite its simplicity, is an effective way to perform a local simulation of the forced convection heat transfer process which occurs when a fluid flows through a porous channel considering only realistic boundary conditions.

While the well known classical (single continuum) energy transfer model [1] describes adequately the thermomechanical behaviour of materials such as steel, water, rubber or air, it is not so appropriate for a local description of the heat transfer process in a flow of a newtonian fluid through a porous medium. Such a description would require the solution (for the fluid) of both Navier-Stokes and energy equations in a domain defined by all active pores. Boundary conditions, such as no-slip condition and prescribed temperature (and/or heat fluxes), should be considered on all pore walls. The currently available tools are not adequate to allow a simulation of so great complexity.

In order to construct a local description, the problem is regarded through a Continuum Theory of Mixtures viewpoint [2]. A binary (solid-fluid) mixture is considered, in which the fluid, represented by the "fluid constituent", is assumed newtonian and incompressible, while the porous medium, represented by the "solid constituent", is assumed rigid, homogeneous, isotropic and at rest.

This model, supported by a theory with thermodynamical consistence, which generalizes the Classical Continuum Mechanics, allows a local description of the heat transfer phenomenon in a porous medium saturated by a fluid.

The forced convection heating of a fluid which flows through a porous channel, bounded by two impermeable isothermal flat plates, is simulated with the aforementioned model.

When the energy transfer between solid and fluid constituents is studied in a Continuum Theory of Mixtures viewpoint, the existence of two temperatures at each spatial point of the domain is allowed (the fluid and the solid constituents temperatures) giving rise to the Energy Generation Function [3] (which describes the thermal interaction between both constituents of the mixture). The Continuum Theory of Mixtures demands each constituent to satisfy a given set of balance equations, while a global set of balance equations must be satisfied by the mixture.

When the forced convection heating of a fluid flowing through a porous channel is considered, in a two-dimensional geometry (as shown in Figure 1), a system of two second-order partial differential equations on both x- and y-variables is to be solved. The characteristic nature of the energy equations allows this

system to be solved with only one boundary condition on x-direction. From a mathematical viewpoint, this statement may sound absurd, but from a physical viewpoint, if both constituents temperatures are prescribed on the channel superior and inferior boundaries (y-direction) and the fluid inlet temperature is known, no additional boundary condition seems necessary to determine both constituents temperature fields. The use of additional boundary conditions could, even, give rise to an unrealistic behaviour near the boundaries.

The main objective of this work is to present a simple, but effective, procedure, capable of selecting the physically expected solution for a system of second-order partial differential equations, in two variables each, employing only five boundary conditions (instead of the usual eight): four on y-direction and only one on x-direction. This procedure can be employed in any situation, provided that the fluid constituent velocity is not zero. The porous channel shown in Figure 1 could be regarded as a simplified packed-bed heat exchanger whose description, using a two-temperatures model, would require the previous knowledge of boundary conditions such as temperature or heat transfer for both constituents, at the channel entrance and exit. These quantities, except for the fluid constituent temperature, are not easily evaluated in heat exchangers, but can be estimated by means of the simple procedure presented in this work.

In fact, the exaustive number of examples taken into consideration has shown that the temperatures in the domain interior are not affected by additional boundary conditions on x-direction, which can lead to unrealistic situations on the boundaries.

Since both constituents energy equations are elliptic, four boundary conditions should, in principle, be prescribed on x-direction. The fluid constituent energy equation, however, because of its physical nature, is treated as a sequence of parabolic equations, suggesting that only one boundary condition (at the channel entrance) seems to be necessary for its solution. Some tests, in which the fluid constituent inlet temperature was known and several values of the solid constituent partial heat flux (defined so as to be proportional to the difference between solid and fluid constituents temperatures) at the channel entrance and exit were used, have confirmed the mentioned expectation.

The coupling of both energy equations suggested a step forward: to prescribe no condition for the solid constituent, neither at the channel entrance nor at its exit. The verification of the possibility to determine the solution of the system with only one boundary condition on x-direction, which allows the phenomenon to be studied in a more (physically) realistic way, has motivated the present work.
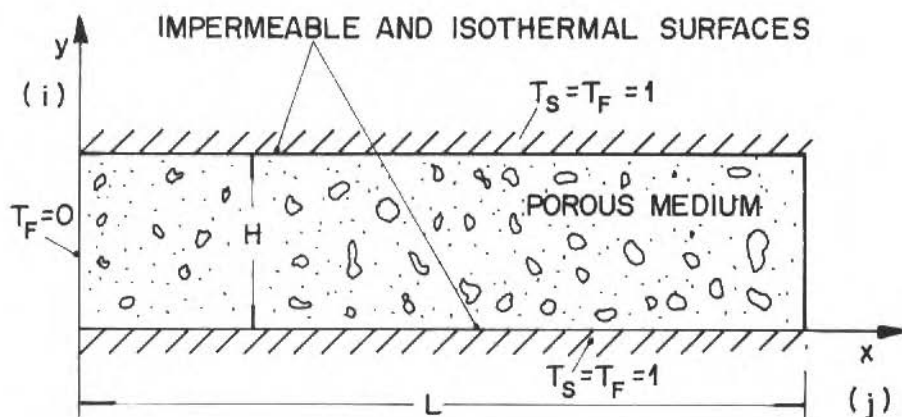
Figure 1. Problem Scheme

MATHEMATICAL MODEL

Considering the mass and linear momentum balance equations for the fluid constituent (the porous medium is assumed rigid and at rest) and the two-dimensional geometry, presented in Figure 1, and one-dimensional steady-state flow, the following velocity profile is obtained:

$$v_F = C \left(1 - \frac{\cosh \frac{y}{\sqrt{K}\lambda}}{\cosh \frac{H/2}{\sqrt{K}\lambda}} \right) \tag{1}$$

for $-H/2 \leq y \leq H/2$, in which C is a constant [4], H the channel width, K the porous medium specific permeability, and λ a parameter depending on the porous matrix.

The energy balance [2] must be satisfied by each constituent of the mixture. Supposing steady-state conditions and zero heat generation for both constituents, it can be stated as:

$$\rho_i c_i(grad\ T_i) \cdot \mathbf{v}_i = -div\ \mathbf{q}_i + \psi_i \tag{2}$$

where $i \equiv S$ and $i \equiv F$ stand for the solid and the fluid constituents, respectively, ρ_i stands for the i-constituent density, T_i for its temperature, $\mathbf{q}_i$ and ψ_i represent, respectively its partial heat flux and energy generation function and, finally, c_i represents the specific heat of the i-constituent, regarded as a continuum.

As the mixture theory viewpoint allows the existence of a different temperature for each constituent, at each spacial point, in order to determine the two temperature fields (T_F and T_S), both energy equations are to be solved.

Equation (2) requires some constitutive hypotheses. The partial heat fluxes for solid and fluid constituents ($\mathbf{q_S}$ and $\mathbf{q_F}$), according to the model used by Saldanha da Gama [3], are stated as:

$$\mathbf{q_S} = -\Lambda k_S(1-\varphi)grad\ T_S \tag{3}$$

$$\mathbf{q_F} = -\Lambda k_F\varphi grad\ T_F$$

where Λ represents an always positive parameter which may depend on both the internal structure and the kinematics of the mixture, k_S and k_F are, respectively, the solid and the fluid thermal conductivities and φ the fluid fraction (coincident to the porosity, for saturated flows).

The total heat flux (per unit of time and area) for the mixture is given by the sum of $\mathbf{q_S}$ and $\mathbf{q_F}$.

The energy generation function, ψ, which is an internal contribution, represents the energy supply to a given constituent, arising from its (thermal) interaction with the other constituents of the mixture. The ψ function is zero at a given point only if all the constituents are at the same temperature at this point. According to Martins Costa [5], the energy generation function for solid and fluid constituents are given by:

$$\psi_S = -\psi_F = R(T_F - T_S) \tag{4}$$

where R is an always positive factor, which represents the heat transfer coefficient between constituents, assumed constant in this work.

Considering these constitutive hypotheses, the balance of energy for the fluid and the solid constituents can be written as:

$$\rho_F c_F (grad\ T_F) \cdot \mathbf{v_F} = \Lambda k_F \varphi \Delta(T_F) + R(T_S - T_F) \tag{5}$$

$$0 = \Lambda k_S (1 - \varphi) \Delta(T_S) + R(T_F - T_S) \tag{6}$$

Since the fluid velocity is non zero only in the x-direction and considering the two-dimensional geometry of the problem, as shown in Figure 1, the balance of energy can be reduced to:

$$\alpha \frac{\partial T_F}{\partial x} = \left[\frac{\partial^2 T_F}{\partial x^2} + \frac{\partial^2 T_F}{\partial y^2} \right] + \beta(T_S - T_F) \tag{7}$$

$$0 = \frac{\partial^2 T_S}{\partial x^2} + \frac{\partial^2 T_S}{\partial y^2} + \gamma(T_F - T_S) \tag{8}$$

where:

$$\alpha = \frac{\rho_F c_F v_F}{\Lambda k_F \varphi}$$

$$\beta = \frac{R}{\Lambda k_F \varphi} \tag{9}$$

$$\gamma = \frac{R}{\Lambda k_S (1 - \varphi)}$$

subject to the following boundary conditions:

$$T_F(0, y) = 0$$

$$T_F(x, 0) = T_S(x, 0) = 1 \tag{10}$$

$$T_F(x, H) = T_S(x, H) = 1$$

NUMERICAL METHOD

The problem consists of a system of two second order equations, on both x and y-variables, subjected to four boundary conditions on y-direction and to

only one boundary condition on x-direction. From a mathematical viewpoint, a problem of this kind, consisting of two elliptic equations, on both x- and y-variables, even if physically realistic, could give rise to an infinite number of solutions. However, a great number of tested situations has shown that additional boundary conditions on x-direction have no influence on both solid and fluid constituents bulk temperatures.

An iterative procedure is used, so that two second-order equations on x-variable can be solved with the help of a single boundary condition on x-direction: the fluid constituent inlet temperature. The problem is treated as a succession of modified problems in which the second-order derivatives on x-direction, for both constituents, are treated as previously known fields, that is: the fluid constituent energy equation is treated as a sequence of parabolic problems on x-variable, while the solid constituent energy equation can be considered as a sequence of ordinary problems on y-variable. This procedure can be summarized in the following way: to start the scheme, initial values are estimated for the second-order derivatives with respect to x. With this the equations below are solved and the temperature fields are calculated. For the following iteractions, the value of $\frac{\partial^2 T_i}{\partial x^2}$ for both constituents are computed from the previous step. The process is carried on until convergence is achieved. The original system of equations is modified to:

$$\left[\alpha \frac{\partial T_F}{\partial x} - \frac{\partial^2 T_F}{\partial y^2} - \beta(T_S - T_F)\right]^l = \left[\frac{\partial^2 T_F}{\partial x^2}\right]^{l-1} \tag{11}$$

$$\left[-\frac{\partial^2 T_S}{\partial y^2} - \gamma(T_F - T_S)\right]^l = \left[\frac{\partial^2 T_S}{\partial x^2}\right]^{l-1} \tag{12}$$

where the derivatives $\frac{\partial^2 T_F}{\partial x^2}$ and $\frac{\partial^2 T_S}{\partial x^2}$ are calculated from the previous iteration.

Since no analytical solution to the system of equations describing the problem is known, numerical approximations to its solution are searched with the help of a finite difference approach [6]. For the diffusive terms, a central finite difference scheme discretization was used, while an "Upwind" scheme [6] was employed in the convective term discretization.

As the temperature coefficients matrix (associated to the modified system of equations) is sparse, a grid description, in which each constituent temperature

possesses two indexes, according to its position on the grid, is used. Each iteration l is then solved with the help of the Gauss-Seidel method, according to the following discretized system:

$$\eta[T_F^{k+1}(i,j)]^l = \delta\{[T_F^{k+1}(i-1,j)]^l + [T_F^k(i+1,j)]^l\}+$$

$$+\nu[T_F^{k+1}(i,j-1)]^l + \beta[T_S^k(i,j)]^l + F\left[\frac{\partial^2 T_F}{\partial x^2}\right]^{l-1} \tag{13}$$

$$\mu[T_S^{k+1}(i,j)]^l = \delta\{[T_S^{k+1}(i-1,j)]^l + [T_S^k(i+1,j)]^l\}+$$

$$+\gamma[T_F^{k+1}(i,j)]^l + F\left[\frac{\partial^2 T_S}{\partial x^2}\right]^{l-1} \tag{14}$$

In (13) and (14), $2 \le i \le Nx$ and $2 \le j \le Ny$, in which Nx and Ny are the number of divisions on x- and y-directions, respectively. The approximations for both constituents second-order partial derivatives, calculated from a previous $(l\text{-}1)$ iteration, are given by the following discretized equations:

$$F\left[\frac{\partial^2 T_F}{\partial x^2}\right]^l \approx \frac{T_F^{l-1}(i,j+1) - 2T_F^{l-1}(i,j) + T_F^{l-1}(i,j-1)}{(\Delta x)^2} \tag{15}$$

$$F\left[\frac{\partial^2 T_S}{\partial x^2}\right]^l \approx \frac{T_S^{l-1}(i,j+1) - 2T_S^{l-1}(i,j) + T_S^{l-1}(i,j-1)}{(\Delta x)^2} \tag{16}$$

where Δx is the mesh size on x-direction, l represents the global iteration, k the Gauss-Seidel iteration and:

$$\eta = \frac{\alpha}{(\delta x)} + \frac{2}{(\delta y)^2} + \beta$$

$$\mu = \frac{2}{(\delta y)^2} + \gamma \tag{17}$$

$$\delta = \frac{1}{(\delta y)^2}$$

$$\nu = \frac{\alpha}{(\delta x)}$$

Equations (13) and (14) represent the modified problem in a very simple way, which allows an effective storage scheme, with memory reutilization.

The iterative procedure, represented by equations (13) to (17), was repeated to a large variety of initial estimate values of the second-order partial derivative on x-direction, ranging from -10^4 to $+10^4$. In all these cases the same results for the solid and fluid constituents temperature fields were obtained, although the rate of convergence showed a slight variation. In some of the tested cases, not only the derivatives initial estimates, but also the factor R (which influences both solid and fluid constituents energy equations coupling) was varied. Convergence to a same set of temperature fields (according to the value of R) was observed for all tested cases. This is a strong argument for the validity of the procedure. Another meaningful argument is that two different sets of similar problems, where the complete energy balance equations are considered (one without the described iterative procedure to calculate the second-order derivative approximations and the other using it only for the fluid constituent) together with different boundary conditions, were simulated and compared to the problem in question. In the first type of problem, several fluid constituent outlet temperatures (ranging from 0 to 1) were prescribed, while zero heat flux was prescribed for the solid constituent both at the channel entrance and exit. For the second type of problem, a similar iterative procedure was used only for the fluid constituent, and several values of the solid constituent heat flux were also considered, both at inlet and outlet, by varying a heat transfer coefficient, h, analogous to the one usually employed in the classical Newton's law of cooling, in equations:

$$A k_S(1 - \varphi)\frac{\partial T_S}{\partial x}(0, y) = h[T_S(0, y) - T_F(0, y)] \qquad (18)$$

$$-\Lambda k_S(1 - \varphi)\frac{\partial T_S}{\partial x}(L, y) = h[T_S(L, y) - T_F(L, y)]$$

In all these cases no alteration on both constituents temperature profile, except for the channel entrance and/or exit, is observed.

The above stated arguments seem sufficient to validate the numerical procedure employed in the present work.

The convergence criterium for both Gauss-Seidel and global iterations was:

$$\max_{(i,j)}\{|T_F^m(i,j) - T_F^{m-1}(i,j)|, |T_S^m(i,j) - T_S^{m-1}(i,j)|\} \leq 10^{-6} \qquad (19)$$

where $1 \leq i \leq (Nx + 1)$, $1 \leq j \leq (Ny + 1)$

A very quick convergence of the global-iterations was observed, four global iterations being sufficient for the worst case. The rate of convergence of the intermediate iterations (Gauss-Seidel method) changed also, according to the second-order partial derivatives initial values.

RESULTS

In this section some results, considering a long porous channel (with length 120 and heigh 1) divided into a 13x13 grid as default, are presented. In Figures 2 and 3 this default problem is compared, respectively to a problem where zero heat flux is prescribed for the solid constituent on both channel extremities, while several values for the fluid constituent outlet temperature are prescribed, and to another problem where two different values of solid constituent heat flux are considered (on both channel extremities) while no boundary condition is imposed to the fluid constituent at the channel exit.

Table 1 represents the convergence process, which can be considered fast, for a point, located at the geometrical center, without loss of generality. Several initial values of second-order partial derivatives on x-direction were used, and the same curves were obtained for the last iteration, indicating convergence independence from initial estimates. This procedure was repeated for other values of the Energy Generation Function (which causes the coupling of both constituents energy equations, acting as a source term) by varying the factor R and using several initial estimates for each considered value of R. In all cases convergence to the same set of temperature fields (one set for each value of R) was obtained.

Figures 4 and 5 plot both constituents temperature (in the channel central point) for different mesh sizes and its percentual difference, related to the most refined grid considered, respectively. Figures 6 and 7 compare the temperature behaviour when mesh size is reduced 50 % on x-direction. In Figure 8 the

Table 1. Convergence Process - Central Point Temperature (for $\frac{\partial^2 T_F}{\partial x^2}$ and $\frac{\partial^2 T_S}{\partial x^2}$ $= 10^4$, $= -10^4$ and $= 0$)

FLUID CONSTITUENT'S CENTRAL POINT TEMPERATURE				
estimate(*)	1st iter.	2nd iter.	3rd iter.	4th iter.
10^4	$.7906 \times 10^3$	.6018	.6053	.6053
0	.6053	.6053	.6053	—
$- 10^4$	$-.7894 \times 10^3$	.6089	.6053	.6053
SOLID CONSTITUENT'S CENTRAL POINT TEMPERATURE				
estimate (*)	1st iter.	2nd iter.	3rd iter.	4th iter.
10^4	$.1132 \times 10^4$	.8827	.8862	.8862
0	.8862	.8862	.8862	—
-10^4	$-.1131 \times 10^4$	.8897	.8862	.8862

(*) initial values for $\frac{\partial^2 T_F}{\partial x^2}$ and $\frac{\partial^2 T_S}{\partial x^2}$

channel length is made five times smaller than the default length and two different values for the fluid constituent mean velocity are considered: the default value, used in the preceding figures and a value ten times smaller. Figure 9 compares the default fluid constituent mean velocity to one ten times greater, using a channel length five times greater than the value considered in Figures 2 to 7. The influence of the fluid constituent mean velocity on both constituents temperatures is shown in Figure 10.

Figure 2 shows both constituents centerline temperatures versus the x-variable in two different cases. The first one (represented by the dashed lines, for both constituent curves) shows the problem, whose simulation originated the present work: no boundary conditions are prescribed either for the fluid constituent at the channel exit or for the solid constituent both at the channel entrance and exit, as stated in equation (10). The continuous curves correspond to the second case, where zero heat flux was prescribed for the solid constituent, both at inlet and outlet. Six different fluid constituent curves correspond to the described solid constituent curve, according to the prescribed outlet fluid constituent temperatures. Several values were considered for this temperature, varying from 0 (the fluid constituent prescribed inlet temperature) to 1 (the impermeable isothermal surfaces prescribed temperature). This second

problem, in which four boundary conditions were prescribed on x-direction, shows an artificial behaviour, both at the channel entrance and exit. Except for these values, complete agreement can be verified between the temperature fields, for both cases taken into consideration.
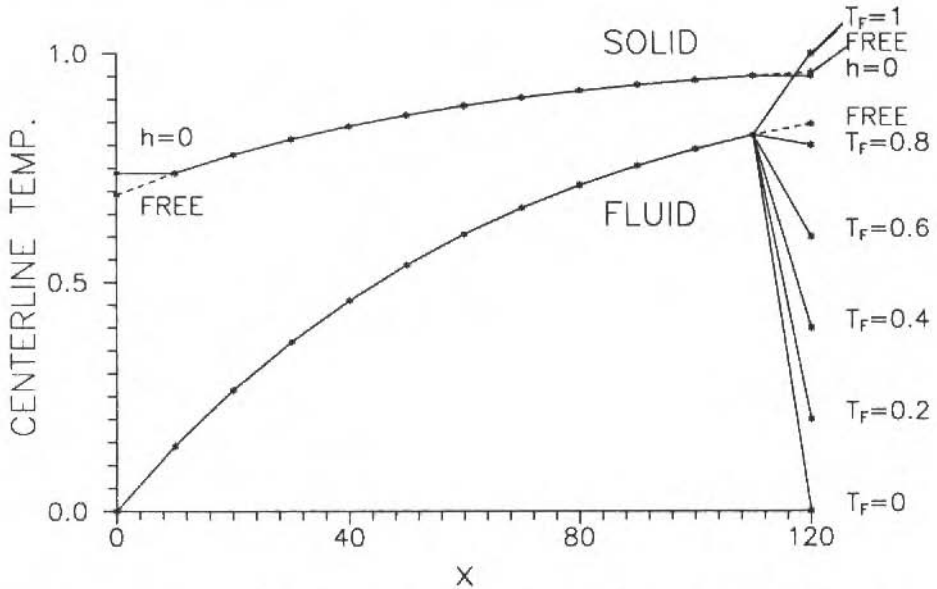
Figure 2. Centerline Temperatures vs x (varying T_F at the channel exit)

Figure 3 shows a comparison between two different problems, the first one, represented by the dashed lines, as in Figure (2), is the one described by equations (7) to (10), while in the other case several heat fluxes are considered, by varying the heat transfer coefficient h in equation (18), for the solid constituent, both at the channel entrance and exit, while no boundary condition for the fluid constituent at the outlet is prescribed. The latter problem, represented by the continuous lines, is solved by means of an iterative scheme, in which the elliptic fluid constituent problem is solved as a sequence of parabolic problems. This scheme is similar to the one described in the present work, but only the fluid constituent second-order partial derivative on x-direction is treated as a known field. It is remarkable that no variation on the fluid constituent temperature curve is observed, when no boundary condition or
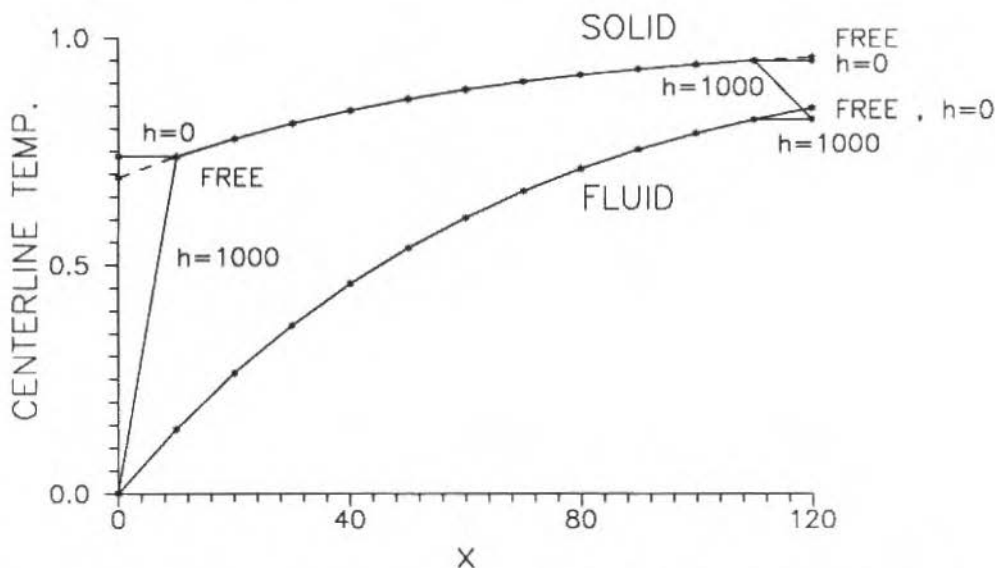
Figure 3. Centerline Temperatures vs x (varying q_S both at inlet and outlet)

zero heat flux was prescribed for the solid constituent. A very slight difference between these mentioned cases is observed at the channel exit, while a more significative difference can be observed at its entrance. The use of a heat transfer coefficient so great as $h = 1000$ is almost equivalent to prescribe both solid and fluid constituents temperatures with the same value. As a consequence, a value very close to zero is observed at the channel entrance for the solid constituent temperature, while apparently the same temperature values for both constituents can be observed at the channel exit. This problem was considered for several values of h, between 0 and 1000, and, except for the channel entrance and exit, no difference on both constituents temperature fields is observed, as occurred on the case shown in Figure 2.

Table 1 shows fluid and solid constituents temperature values at the geometrical center of the channel, that is, for $x = 60$ and $y = 0.5$, for the four global iterations, requested to obtain convergence, in the worst cases. Three different values for solid and fluid partial second-order derivatives on x-direction, among the several ones used as initial values, were chosen to be listed. Significative

differences can be observed between first and second iterations, when the derivative initial values are considered 10^4 or -10^4, while almost no difference is observed if second and third iterations are compared. If the derivatives are initialized as zero, only three global iterations are requested to achieve convergence. An analogous behaviour is verified if the fluid constituent mean velocity is made 1000 times smaller: convergence is reached after three global iterations, if both derivatives are initialized as zero, while five global iterations are requested if they are initialized as -10^4 or 10^4
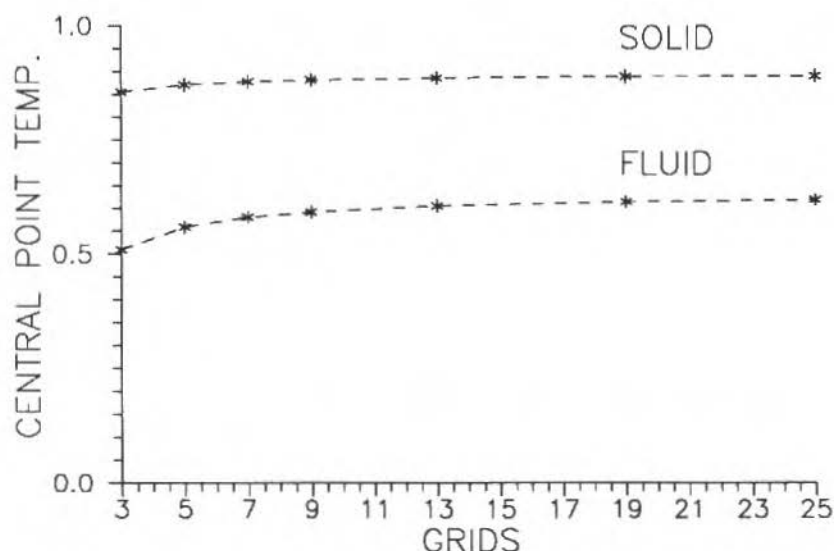
Figure 4. Central Point Temperatures (for different mesh sizes)

Figure 4 shows both constituents temperatures at a point located at the centerline center, for different meshes, from a 3x3 to a 25x25 mesh. The percentual difference among the latter mesh and the remaining ones, at the central point, is plotted for both constituents temperatures in Figure 5. Examining Figures 4 and 5 together, it can be noticed that the 13x13 grid, used for the majority of the results presented in this work, shows a reasonable
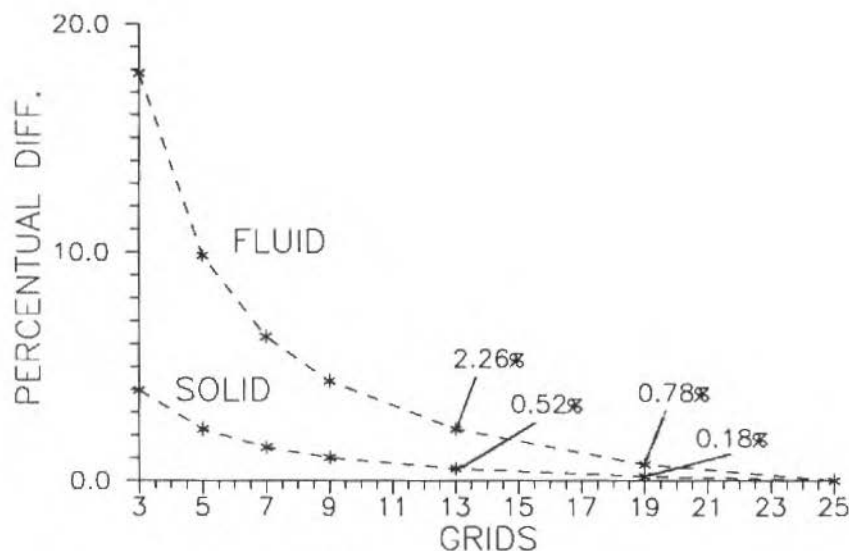
Figure 5. Percentual Difference among Central point Temperature (for different mesh sizes, related to the most refined grid)

agreement to the most refined one used: the 25x25 grid, for both constituents temperatures.

Figure 6 shows both constituents centerline temperatures for two different mesh sizes: 25x13 and 13x13. A very slight difference is observed for the fluid constituent temperature, while almost no difference can be noticed for the solid constituent , as the grid is refined on x-direction. The same grids are compared in Figure 7, where both constituents temperatures are plotted for a section $x = 110$, near the channel exit, where the difference between the curves representing the two considered mesh sizes is more acute as it can be seen in Figure 6.

Figures 8 and 9 represent both constituents centerline temperatures versus x-variable for different values of the channel length and different fluid constituent mean velocities. In Figure 8 the channel length is five times smaller than the default value ($L = 24$) and the average velocities are considered 10^{-3} (the
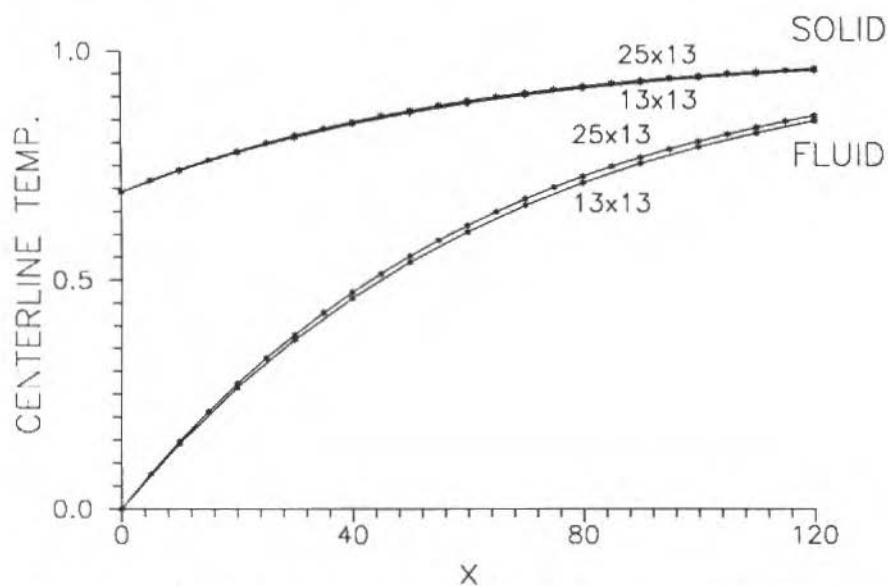
Figure 6. Centerline Temperatures vs x (for 25x13 and 13x13 grids)
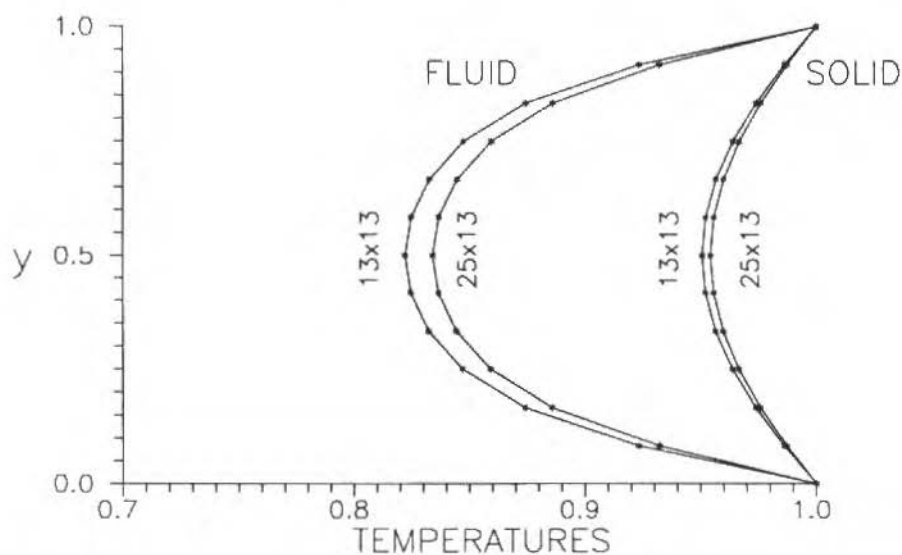
Figure 7. Temperature vs y - Section $x = 18.5$ (for 25x13 and 13x13 grids)

default value) and 10^{-4}. A significative difference between both constituents centerline temperatures can be observed for the default velocity, while these temperatures tend to a common value at the channel exit, for an average velocity ten times smaller. An analogous behaviour is noticed in Figure 9, in which the channel length is five times greater than the default value ($L = 600$): both constituents centerline temperatures are almost coincident at the second half of the channel for the default fluid constituent average velocity (10^{-3}) but they show a large difference if the mean velocity is made ten times greater (10^{-2}). Comparing these two figures to Figure 6, in which $L = 120$, a fully developed temperature field, for a given mean velocity, becomes a natural expectation.
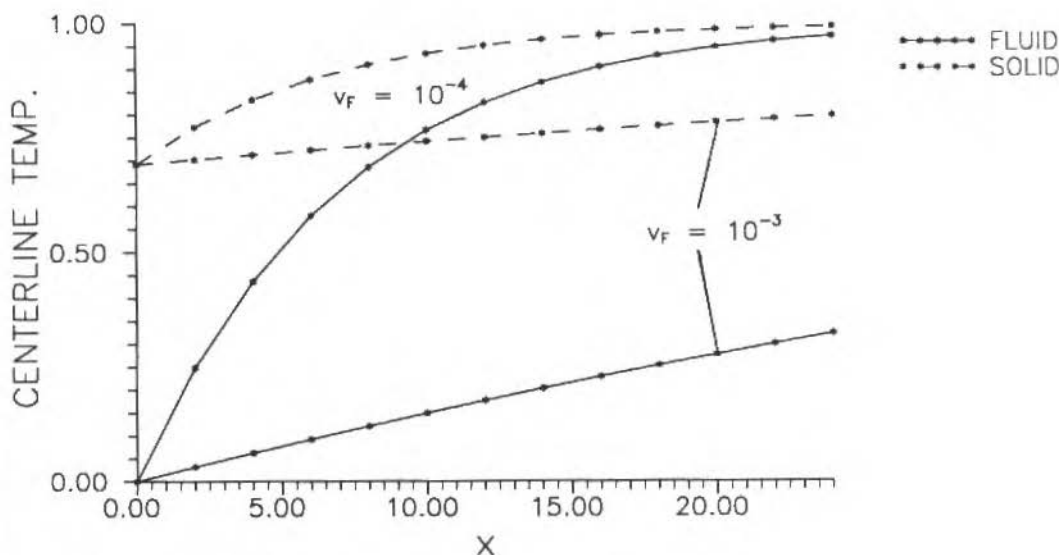
Figure 8. Centerline Temperatures vs x (for $L = 24$ and two mean values for v_F)

Figure 10 illustrates the influence of the fluid constituent mean velocity on both constituents centerline temperatures. It can be seen that a decrease on the mean velocity makes both constituents centerline temperatures tend
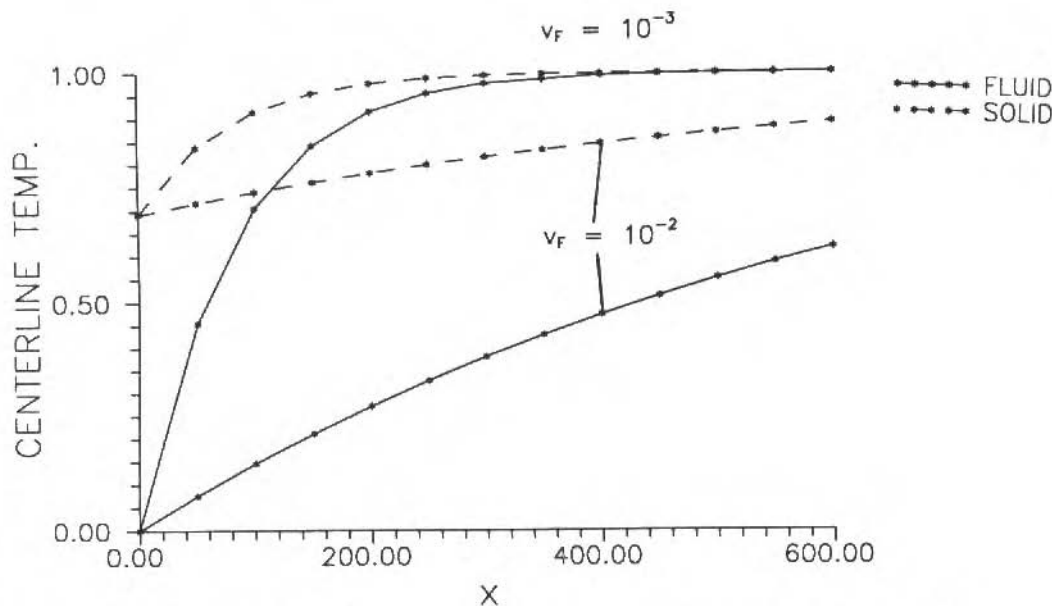
Figure 9. Centerline Temperatures vs x (for $L = 600$ and two mean value for v_F)

to a common value. (For average velocities of 10^{-6} or 10^{-7}, both curves are coincident, except at the channel entrance, where the fluid constituent temperature is prescribed. On the other hand, for an average velocity of 1, T_F is almost zero and T_S almost constant.) This leads to the conclusion that as the fluid constituent mean velocity decreases, thermal equilibrium between constituents is reached after a shorter channel length.

The effect of the fluid constituent mean velocity on both constituents temperatures can be regarded in a simpler way, using the new variables $x^* = \alpha x$ and $y^* = \alpha y$, in equations (7) and (8), which become:

$$\frac{\partial T_F}{\partial x^*} = \left[\frac{\partial^2 T_F}{\partial (x^*)^2} + \frac{\partial^2 T_F}{\partial (y^*)^2} \right] + \frac{\beta}{\alpha^2}(T_S - T_F) \tag{20}$$

$$0 = \frac{\partial^2 T_S}{\partial (x^*)^2} + \frac{\partial^2 T_S}{\partial (y^*)^2} + \frac{\gamma}{\alpha^2}(T_F - T_S)$$
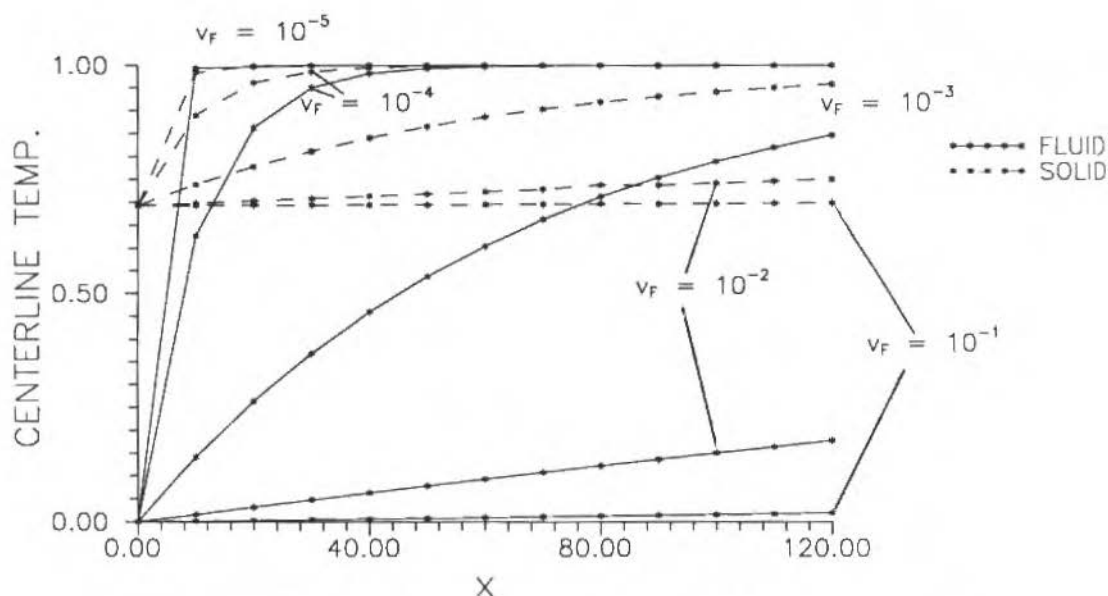
Figure 10. Centerline Temperatures vs x (varying fluid constituent mean velocity)

Using these new equations, in which the factor α may be regarded as a "geometric scaling factor", a variation on the channel length would include effects of variation of the fluid constituent velocity on both constituents temperatures, shown in Figures 8 to 10.

ADDITIONAL COMMENTS

Figure 11 shows centerline temperatures vs position x for two different cases: the default problem, represented by equations (7) to (10), and an alternative problem, where equations (7) and (8) are subjected to another set of boundary conditions: zero heat flux, instead of temperature, is prescribed for the fluid constituent on both impermeable surfaces, so that instead of equation (10), the boundary conditions become:

$$T_F(0, y) = 0$$

$$\frac{\partial T_F}{\partial y}(x,0) = \frac{\partial T_F}{\partial y}(x,H) = 0 \qquad (21)$$

$$T_S(x,0) = T_S(x,H) = 1$$

The same previously described procedure was used to solve this problem, and convergence was obtained in three global iterations, as occurred to equations (7) to (10), if both fluid and solid constituents partial derivatives on x-direction initial estimates were zero. Examining Figure 11 it is observed that the curves describing the two mentioned cases are almost coincident. This means that an alteration on the fluid constituent boundary condition on y-direction from prescribed temperature to zero heat flux causes almost no alteration on both constituents centerline temperatures. Significative variation is noticed only if fluid constituent cross sections temperatures are compared for both cases, as shown in Figure 12, where a central section ($x = 60$) is considered.
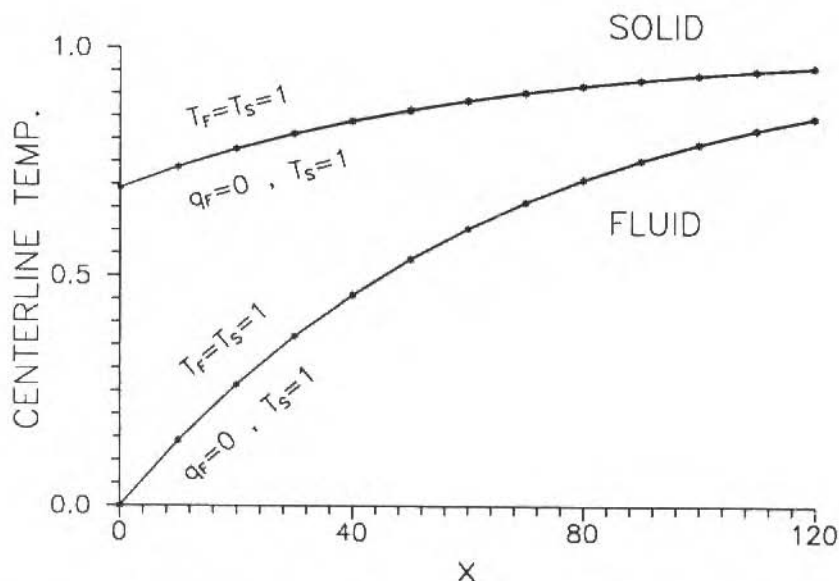
Figure 11. Centerline Temperatures vs x (varying boundary conditions on y-direction)
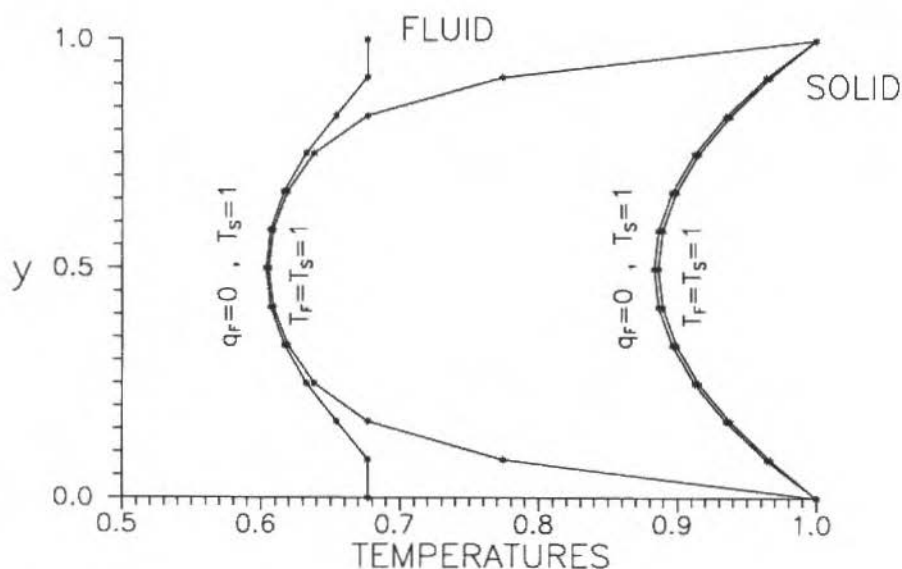
Figure 12. Temperature vs y - Section $x = 60$ (varying boundary conditions on y-direction)

FINAL REMARKS

When a problem like the one stated in equations (7) and (8) is simulated, usually a total of eight boundary conditions is required. However, the practical situation considered in the present work becomes unrealistic if all the usual boundary conditions are prescribed.

This work presents an algorithm which allows the local simulation of the energy transfer process in a saturated flow through a rigid porous medium, using a Mixtures Theory viewpoint, in which a system of two elliptic equations on both x- and y-variables are solved with only one boundary condition on x-direction: the fluid constituent inlet temperature. Additional data like the fluid constituent temperature or heat transfer and the solid constituent inlet and outlet temperature and/or heat transfer, which are not available in practical problems, need not to be known.

Some previous works (e. g. Vafai and Sozen [7] and Lage and Bejan [8]) have already used a two-temperatures model to describe the momentum and heat transfer process in saturated porous media. These models, obtained from a Continuum Mechanics approach, present a term, analogous to the energy generation function, which takes into account solid and fluid temperature differences. Both temperatures, however, are calculated as intrinsic volume averages, each one in a volume associated to the respective phase. (As the Mixtures Theory basic hypothesis states that each constituent occupies the whole volume of the mixture, the intrinsic volume can be the same for both phases, in this case.)

REFERENCES

[1] SLATTERY, J. C., *Momentum, Energy and Mass Transfer in Continua*, 2nd edn, Robert E. Krieger Publishing Co., New York, 1981.

[2] ATKIN, R.J. and CRAINE, R.E., 'Continuum Theories of Mixtures: Basic Theory and Historical Development', Quart. J. Mech. Appl. Math., **29**, 209-244 (1976).

[3] SALDANHA DA GAMA, R.M., 'A Model for Heat Transfer in Rigid Continuous Mixtures', Int. Comm. Heat Mass Transfer, **16**, 123-132 (1989).

[4] MARTINS COSTA, M. L., SAMPAIO, R. and SALDANHA DA GAMA, R. M., 'Local description of the Energy Transfer Process in a Packed Bed Heat Exchanger', Proceedings of the III National Meeting on Thermal Sciences (ENCIT), **2**, 689-693, Itapema, SC, Brazil (1990).

[5] MARTINS COSTA, M. L., 'Modelling and Simulation of the Energy Transfer in Saturated Porous Media by using Theory of Mixtures', (In Portuguese), DSc. Thesis, Pontifícia Universidade Católica do Rio de Janeiro, Brazil, 1991.

[6] EUVRARD, D., *Résolution Numérique des Équations aux Derivées Partielles*, Masson, Paris, 1987.

[7] VAFAI, K. and SOZEN, M., ' Analysis of Energy and Momentum Transport for Fluid Flow through a Porous Bed', J. Heat Transfer, **112**, 690-699 (1990).

[8] LAGE, J. L. and BEJAN, A., 'Numerical Study of Forced Convection near a Surface Covered with Hair', Int. J. Heat Fluid Flow, **11**, 242-248 (1990).

ON SOME INTEGRAL REPRESENTATIONS OF THE KERNEL FUNCTION OCCURRING IN UNSTEADY SUBSONIC POTENTIAL FLOWS

REPRESENTAÇÕES INTEGRAIS DA FUNÇÃO DO NÚCLEO DO ESCOAMENTO POTENCIAL NÃO ESTACIONÁRIO EM REGIME SUBSÔNICO

Maher N. Bismarck-Nasr - Membro da ABCM
Divisão de Engenharia Aeronáutica
Instituto Tecnológico de Aeronáutica
12225, São José dos Campos, SP, Brazil

ABSTRACT

Integral representations of the function of the non-elementary part of the Kernel of the integral equation relating the pressure to the normalwash distribution occurring in unsteady subsonic potential flows are presented. Several integral transforms are deduced from these integral representations. The results obtained can be extended to other fields of application and, therefore, are not limited to the solution of unsteady potential flow problems.

Keywords: Unsteady Subsonic Flows ■ Integral Representations

RESUMO

São apresentadas representações integrais da parte não elementar da função do núcleo da equação integral, em escoamento subsônico potencial não estacionário, que relacionam a diferença de pressão à distribuição da velocidade normal. São deduzidas transformações integrais a partir destas representações integrais. Os resultados podem ser estendidos à outros campos de aplicação e, portanto, não estão limitados à solução do problema do escoamento potencial não estacionário.

Palavras-chave: Escoamento Subsônico Não Estacionário ■ Representações Integrais

NOMENCLATURE

$Ci(x)$	Cosine integral function
$E_1(x)$	Exponential integral function $= \int_x^\infty \frac{e^{-t}}{t}\, dt$
$E_i(x)$	Complementary exponential function $= \int_{-\infty}^x \frac{e^t}{t}\, dt$
$\mathcal{F}_\nu(x)$	Function defined in equation (7)
$f(x)$	First auxiliary function of the trigonometric integral function $= Ci(x)\sin(x) - si(x)\cos(x)$
$g(x)$	Second auxiliary function of the trigonometric integral function $= -Ci(x)\cos(x) - si(x)\sin(x)$
$H_\mu(x)$	Struve function of order μ
$h_\mu(x)$	$H_\mu(x) - Y_\mu$
i	$\sqrt{-1}$
$I_\mu(x)$	Modified Bessel function of first kind and order μ
$J_\mu(x)$	Bessel function of first kind and order μ
k	reduced frequency, considered as a constant real non-negative parameter $= \frac{\omega\, r}{U_\infty}$
$\mathcal{K}$	Kernel function relating normalwash at point (x, y, z) to unit pressure difference at point (ξ, η, ζ)
$K_\mu(x)$	Modified Bessel function of second kind and order μ
$L_\mu(x)$	Modified Struve function of order μ
$\mathcal{L}_\mu(x)$	$= I_\mu(x) - L_\mu(x)$
M_∞	free stream Mach number
$\mathcal{N}_\nu(x)$	Function defined in equation (6)
q_∞	Free stream dynamic pressure $= \frac{1}{2}\rho_\infty U_\infty^2$
R	$\sqrt{x_o^2 + \beta^2 r^2}$
r	$\sqrt{(y - \eta)^2 + (z - \zeta)^2}$
$Si(x)$	Sine integral function
$si(x)$	$= Si(x) - \frac{\pi}{2}$
U_∞	Free stream velocity in x direction
u	Real argument $= \frac{M_\infty R - x_o}{\beta^2 r}$
$w(x, y, z)$	Normal velocity at point (x, y, z)
(x, y, z)	Coordinates of the normalwash point
(x_o, y_o, z_o)	$(x - \xi, y - \eta, z - \zeta)$
$Y_\mu(x)$	Bessel function of second kind and order μ
α_μ	$= \frac{2^\mu\, \Gamma(\nu)}{\sqrt{\pi}}$
β	$\sqrt{1 - M_\infty^2}$

$\Gamma(x)$	Gamma function
γ	Local dihedral angle
Δp	Pressure difference
ρ_∞	Free stream air density
$\phi(x)$	First auxiliary function of the exponential integral functions
	$= e^x E_1(x) + e^{-x} E_i(x)$
$\psi(x)$	Second auxiliary function of the exponential integral functions
	$= e^x E_1(x) - e^{-x} E_i(x)$
(ξ, η, ζ)	Coordinates of the doublet point
ω	Frequency of oscillation
$(\ )_r$	Receiving point
$(\ )_s$	Sending point
$(\ )_\mu$	$0,1,2,3,\ldots$
$(\ )_\nu$	$\frac{1}{2}, \frac{3}{2}, \frac{5}{2}, \frac{7}{2}, \cdots \quad = \mu + \frac{1}{2}$
$(\ )'$	$\frac{d}{du}$

INTRODUCTION

Since the Küssner[1] derivation of the integral equation relating the pressure to the normalwash distribution in subsonic unsteady potential flows, many authors[2-5] contributed to the reduction of this equation to forms suitable for numerical computations. Many numerical approximations were proposed for the evaluation of the non-elementary part of the Kernel function[2,3,6,7]. These approximate solutions have an accuracy of two to three digits and are time consuming in terms of computational efforts. Exact solutions of the involved integrals of the Kernel function were presented in reference [8]. The solutions presented have been obtained in terms of new functions and efficient numerical evaluation of these functions have been proposed[8]. In reference [9] the unsteady supersonic flow case has been treated and it is shown that the solution of the non-elementary part of the supersonic Kernel is related to the same functional solutions of the subsonic Kernel. Further, reference [9] gives simple and direct expressions for the evaluation of the supersonic Kernel.

The present paper presents several integral representations of these functional solutions. Further, some new integral transforms deduced from these integral representations are given. These new integral representations and integral transforms are connected to the Bessel and Struve functions. These functions

are of great importance in applied mathematics and mechanics, and their integral transforms and integral representations appear in many fields of engineering sciences, e.g., elastic vibrations, potential flows, heat and mass transfer, electromagnetic field problems, etc. It is believed that the results obtained in the present paper will be useful in such engineering applications.

STATEMENT OF THE PROBLEM

The integral equation relating the pressure and the normalwash can be written as[1],

$$\frac{w(x,y,z)}{U_\infty} = \frac{1}{8\pi} \iint \left[\Delta p(\xi,\eta,\zeta) \, \frac{K(\xi,\eta,\zeta;x,y,z;k,M_\infty)}{q_\infty r^2} \right] d\xi \, d\eta \qquad (1)$$

The Kernel function K reads,

$$K = e^{-i\omega x_o/U_\infty} (K_1 T_1 + K_2 T_2) \qquad (2)$$

where T_1 and T_2 are geometric relations and read[4,5]

$$T_1 = \cos(\gamma_r - \gamma_s) \qquad (3a)$$

$$T_2 = \frac{1}{r^2} (z_o \cos \gamma_r - y_o \sin \gamma_r)(z_o \cos \gamma_s - y_o \sin \gamma_s) \qquad (3b)$$

and K_1 and K_2 are given by

$$K_1 = \frac{M_\infty r e^{-iku}}{R\sqrt{1+u^2}} + \mathcal{N}_{3/2}(u) \qquad (4a)$$

$$K_2 = -\frac{ik M_\infty^2 r^2 e^{-iku}}{R^2\sqrt{1+u^2}} - 3\,\mathcal{N}_{5/2}(u)$$

$$- \frac{M_\infty r e^{-iku} \left[(1+u^2)\beta^2 r^2 + 2R^2 + M_\infty R r u \right]}{R^3 (1+u^2)^{3/2}} \qquad (4b)$$

where

$$\mathcal{N}_{3/2}(u) = \int_u^\infty \frac{e^{-ikv}}{(1+v^2)^{3/2}}\, dv = \mathcal{N}_{\mathrm{Re}_{3/2}}(u) + i\,\mathcal{N}_{\mathrm{Im}_{3/2}}(u) \qquad (5a)$$

$$\mathcal{N}_{5/2}(u) = \int_u^\infty \frac{e^{-ikv}}{(1+v^2)^{5/2}} \, dv = \mathcal{N}_{\mathrm{Re}_{5/2}}(u) + i \, \mathcal{N}_{\mathrm{Im}_{5/2}}(u) \tag{5b}$$

Consider now the integral,

$$\mathcal{N}_\nu(u) = \int_u^\infty \frac{e^{-ikv}}{(1+v^2)^\nu} \, dv = \mathcal{N}_{\mathrm{Re}_\nu}(u) + i \, \mathcal{N}_{\mathrm{Im}_\nu}(u) \tag{6}$$

where k is considered as a constant non-negative parameter, $\nu = \frac{1}{2}, \frac{3}{2}, \frac{5}{2}, \frac{7}{2}, \cdots$ and defining the function $\mathcal{F}_\nu(u)$ as[8],

$$\mathcal{F}_\nu(u) = \mathcal{N}_{\mathrm{Re}_\nu}(u) \sin(ku) + \mathcal{N}_{\mathrm{Im}_\nu}(u) \cos(ku) \tag{7}$$

and using equation (5), it can be shown that the function $\mathcal{F}_\nu(u)$ satisfies the differential equation,

$$\mathcal{F}_\nu''(u) + k^2 \mathcal{F}_\nu(u) = -\frac{k}{(1+u^2)^\nu} \tag{8}$$

with the following boundary conditions,

$$\alpha_\mu \mathcal{F}_\nu(0) = (-1)^{\mu+1} \frac{\pi}{2} k^\mu \mathcal{L}_{-\mu}(k) \tag{9a}$$

$$\alpha_\mu \mathcal{F}_\nu'(0) = k^{\mu+1} K_\mu(k) \tag{9b}$$

and recurrence relations[8],

$$4\nu(1+\nu)\mathcal{F}_{\nu+2}(u) = k^2 \mathcal{F}_\nu(u) + 2\nu(2\nu+1)\mathcal{F}_{\nu+1}(u) + \frac{k}{(1+u^2)^\nu} \tag{10}$$

The solution for $\mathcal{F}_\nu(u)$ was given in reference [8] and efficient evaluation of these functions were treated. Further, an integral representation for $\mathcal{F}_\nu(u)$ was given and reads[8],

$$\alpha_\mu \mathcal{F}_\nu(u) = -k \int_0^\infty t^\mu J_\mu(t) \frac{e^{-ut}}{t^2+k^2} \, dt \tag{11}$$

Once the function $\mathcal{F}_\nu(u)$ has been obtained, the integrals given in equation (6) can be evaluated from,

$$\mathcal{N}_{\mathrm{Re}_\nu}(u) = \mathcal{F}_\nu(u) \sin(ku) + \frac{1}{k} \mathcal{F}_\nu'(u) \cos(ku) \tag{12a}$$

$$\mathcal{N}_{\text{Im}_\nu}(u) = \mathcal{F}_\nu(u)\cos(ku) - \frac{1}{k}\mathcal{F}'_\nu(u)\sin(ku) \tag{12b}$$

INTEGRAL REPRESENTATIONS OF $\mathcal{F}_\nu(u)$ IN TERMS OF THE STRUVE FUNCTION

Consider the integral representation of the Bessel function of the first kind[10,11],

$$J_\mu(t) = \frac{t^\mu}{\alpha_\mu \pi} \int_0^\pi \sin^{2\mu}\theta \ [\cos(t\cos\theta)]\ d\theta \tag{13}$$

and the Fourier cosine transform[12],

$$e^{ut} = \frac{2u}{t} \int_0^\infty \frac{\cos(tx)}{x^2 + u^2}\ dx \quad \text{for } u > 0 \tag{14}$$

Substituting equations (13) and (14) into the integral representation of $\mathcal{F}_\nu(u)$ given in equation (11), and changing the order of integration, we obtain,

$$\mathcal{F}_{1/2}(u) = -f(ku)\mathcal{L}_0(k) - \frac{k}{\pi}\int_0^\infty \frac{H_0(t)\,\phi(ut)}{t^2 + k^2}\ dt \tag{15a}$$

$$\mathcal{F}_{3/2}(u) = -k\,f(ku)\mathcal{L}_1(k) - \frac{k}{\pi}\int_0^\infty \frac{t\,H_1(t)\,\phi(ut)}{t^2 + k^2}\ dt \quad \text{for } u > 0 \tag{15b}$$

Higher order relations can be obtained using equations (15), the recurrence relations of the Bessel and Struve functions, and the recurrence relation of $\mathcal{F}_\nu(u)$. The limitation of $u > 0$ is because of equation (14).

Now, using the differential equation (8) and equations (15), the following H_ν transforms of the auxiliary exponential integral functions are obtained:

$$\int_0^\infty H_0(t)\,\phi(ut)\,dt = -\frac{\pi}{\sqrt{1 + u^2}}$$

$$\int_0^\infty H_0(t)\,\psi(ut)\,dt = -\frac{\pi}{u\sqrt{1 + u^2}}$$

$$\int_0^\infty \frac{H_1(t)\,\phi(ut)}{t}\,dt = \pi\left[\sqrt{1 + u^2} - u\right]$$

$$\int_0^\infty \frac{H_1(t)\,\psi(u\,t)}{t}\,dt = \pi\left[\frac{1}{\sqrt{1+u^2}} - \frac{1}{u}\right] \quad \text{for } u > 0 \qquad (16)$$

and the following relations are verified[12]:

$$\mathcal{L}_0(k) = \frac{2}{\pi}\int_0^\infty \frac{t\,H_0(t)}{t^2+k^2}\,dt = \frac{2\,k}{\pi}\int_0^\infty \frac{J_0(t)}{t^2+k^2}\,dt$$

$$\mathcal{L}_1(k) = \frac{2\,k}{\pi}\int_0^\infty \frac{H_1(t)}{t^2+k^2}\,dt = \frac{2\,k^2}{\pi}\int_0^\infty \frac{J_1(t)}{t\,(t^2+k^2)}\,dt \qquad (17)$$

To the author's knowledge, the relations given in equations (15) and (16) are new.

INTEGRAL REPRESENTATIONS OF $\mathcal{F}_\nu(u)$ IN TERMS OF THE MODIFIED BESSEL FUNCTIONS OF THE SECOND KIND

Consider the integral representation of the Struve function[12],

$$h_\mu(t) = \frac{2\,t^\nu}{\pi\,\alpha_\mu}\int_0^\infty e^{-t\,x}\left(1+x^2\right)^{\mu-1/2}\,dx \qquad (18)$$

and the Hankel-Nicholson transform[11,12],

$$h_\mu(t) = \left[(-1)^\mu \frac{4\,t^{\nu+1}}{\pi^2}\right]\int_0^\infty \frac{K_\mu(x)}{x^\mu\,(x^2+t^2)}\,dx \qquad (19)$$

Applying Laplace transform operations on equation (8) and using the integral relations (18) and (19) and the recurrence relation of $\mathcal{F}_\nu(u)$, equation (10), we obtain

$$\alpha_\mu\,\mathcal{F}_\nu(u) = \left[(-1)^{\mu+1}\frac{\pi\,k^\mu}{2}\right]\mathcal{L}_{-\mu}(k)\,\cos(ku) + k^\mu\,K_\mu(k)\,\sin(ku)$$

$$+ \frac{2\,k}{\pi}\int_0^\infty t^\mu\,K_\mu(t)\,\frac{\cos(ku)-\cos(tu)}{k^2-t^2}\,dt \qquad (20)$$

Using now equation (20) and the differential equation (8), the following K_μ transform is verified:

$$\int_0^\infty t^\mu\,K_\mu(t)\,\cos(tu)\,dt = \frac{\pi\,\alpha_\mu}{2\,(1+u^2)^\nu} \qquad (21)$$

Consider now the Fourier cosine transform[12],

$$e^{-ut} = \frac{2t}{\pi} \int_0^\infty \frac{\cos(ux)}{t^2 + x^2}\, dx \quad \text{for } u > 0 \qquad (22)$$

Substituting equation (22) into the integral representation of $\mathcal{F}_\nu(u)$, equation (11), changing the order of integration, and using equation (27) of reference [8], we obtain

$$\alpha_\mu\, \mathcal{F}_\nu(u) = \frac{2k}{\pi} \int_0^\infty \left[k^\mu K_\mu(k) - t^\mu K_\mu(t) \right] \frac{\cos(tu)}{k^2 - t^2}\, dt \quad \text{for } u > 0 \qquad (23)$$

Using now equations (23) and (20), the following K_μ transform is obtained:

$$\int_0^\infty \frac{t^\mu K_\mu(t)}{k^2 - t^2}\, dt = (-1)^\nu\, \frac{\pi^2}{4}\, k^{\mu-1}\, \mathcal{L}_{-\mu}(k) \qquad (24)$$

and, therefore, from equation (24) and equation (20) or equation (23), we obtain

$$\alpha_\mu\, \mathcal{F}_\nu(u) = k^\mu K_\mu(K)\, \sin(ku) - \frac{2k}{\pi} \int_0^\infty t^\mu K_\mu(t)\, \frac{\cos(tu)}{k^2 - t^2}\, dt \quad \text{for } u > 0 \quad (25)$$

The relationships given in equations (20), (23), and (25) connect the new function $\mathcal{F}_\nu(u)$ to integral transforms of the modified Bessel functions of the second kind. Therefore, these integral transforms can be evaluated in terms of $\mathcal{F}_\nu(u)$.

INTEGRAL REPRESENTATIONS OF $\mathcal{F}_\nu(u)$ IN TERMS OF THE MODIFIED BESSEL AND STRUVE FUNCTIONS

Consider the integral representation of the auxiliary exponential function[12],

$$\phi(ut) = 2t \int_0^\infty \frac{\sin(ux)}{x^2 + t^2}\, dx \qquad (26)$$

Substituting equation (26) into equation (15), and changing the order of integration, we obtain

$$\mathcal{F}_{1/2}(u) = f(ku)\, \mathcal{L}_0(k) - k \int_0^\infty \sin(ut) \frac{\mathcal{L}_0(k) - \mathcal{L}_0(t)}{t^2 - k^2}\, dt \qquad (27a)$$

$$\mathcal{F}_{3/2}(u) = -k\left[\sqrt{1+u^2} - u\right] + k\,f(ku)\,\mathcal{L}_1(k)$$

$$+ k^2 \int_0^\infty \sin(ut)\frac{t\,\mathcal{L}_1(k) - k\,\mathcal{L}_1(t)}{t\,(t^2 - k^2)}\,dt \qquad (27b)$$

Higher order relations can be obtained using equations (27), the recurrence relation of $\mathcal{F}_\nu(u)$, equation (11), and the recurrence relations of the modified Bessel and Struve functions.

Now, using the Fourier sine transform[12],

$$\int_0^\infty \frac{\sin(ut)}{k^2 - t^2}\,dt = \frac{1}{k}\,f(ku) - \frac{\pi}{2}\,\cos(ku) \qquad (28)$$

in equation (27), we obtain

$$\mathcal{F}_{1/2}(u) = -\frac{\pi}{2}\,\cos(ku)\,\mathcal{L}_0(k) - k\int_0^\infty \sin(ut)\frac{\mathcal{L}_0(t)}{k^2 - t^2}\,dt \qquad (29a)$$

$$\mathcal{F}_{3/2}(u) = -k\left[\sqrt{1+u^2} - u\right] + \frac{\pi\,k}{2}\,\cos(ku)\,\mathcal{L}_1(k)$$

$$+ k^3 \int_0^\infty \sin(ut)\frac{\mathcal{L}_1(t)}{t\,(k^2 - t^2)}\,dt \qquad (29b)$$

Applying the differential equation (8) on equations (29), we obtain the following transforms:

$$\int_0^\infty \sin(ut)\,\mathcal{L}_0(t)\,dt = \frac{1}{\sqrt{1+u^2}} \qquad \text{for } u > 0 \qquad (30a)$$

$$\int_0^\infty \sin(ut)\frac{\mathcal{L}_1(t)}{t}\,dt = \sqrt{1+u^2} - u \qquad \text{for } u > 0 \qquad (30b)$$

Now, consider the Fourier sine transform[12],

$$e^{-ut} = \frac{2}{\pi}\int_0^\infty \frac{x\,\sin(ux)}{x^2 + t^2}\,dx \qquad \text{for } u > 0 \qquad (31)$$

Substituting equation (31) into the integral representation of $\mathcal{F}_\nu(u)$, equation (11), and using equation (26) of reference [8], we obtain,

$$(-1)^\mu\,a_\mu\,\mathcal{F}_\nu(u) = k\int_0^\infty t\,\sin(ut)\frac{t^{\mu-1}\,\mathcal{L}_{-\mu}(t) - k^{\mu-1}\,\mathcal{L}_{-\mu}(k)}{t^2 - k^2}\,dt$$

$$\text{for } u > 0 \tag{32}$$

and

$$(-1)^{\mu} \alpha_{\mu} \mathcal{F}_{\nu}(u) = -\frac{\pi}{2} k^{\mu} \mathcal{L}_{-\mu}(k) \cos(ku)$$

$$- k \int_{0}^{\infty} t^{\mu} \sin(ut) \frac{\mathcal{L}_{-\mu}(t)}{k^2 - t^2} \, dt \tag{33}$$

The relationships given in equations (27), (29), (32), and (35) connect the new function F_{ν} to integral transforms of the modified Bessel and Struve functions. Therefore, these integral transforms can be evaluated in terms of F_{ν}. To the author's knowledge, the integral representation given in equations (30) are new.

CONCLUSIONS

Integral representations of the function of the non-elementary part of the Kernel of the integral equation relating the pressure to the normalwash distribution occurring in unsteady subsonic potential flows have been presented. It is believed that these integral representations will be useful for evaluating the integrations given in terms of the function $F_{\nu}(u)$. The results obtained can be extended to other fields of application and, therefore, are not limited to the solution of unsteady potential flow problems.

ACKNOWLEDGEMENTS

REFERENCES

[1] KÜSSNER, II. G., "Allgemeine Tragflachentheorie", *Luftfahrtforschung*, Vol. 17, N. 11-12, pp. 370-379, 1940, see also, "General Airfoil Theory", NACA TM-979, 1941.

[2] WATKINS, C. E., RUNYAN, II. L., and WOOLSTON, D. S., "On the Kernel Function of the Integral Equation Relating the Lift and the Downwash Distribution of Oscillating Finite Wings in Subsonic Flows", NACA Report 1234, 1955.

[3] LASCHKA, B., "Zur Theorie der Harmonisch Schwingenden Tragenden Flache bei Unterschallanstromung", *Zeitschrift für Flugwissenschaften*, Vol. 11, N. 7, pp. 265-292, 1963.

[4] LANDAHL, M. T., "Kernel Function for Nonplanar Oscillating Surfaces in Subsonic Flow", *AIAA Journal*, Vol. 5, N. 5, pp. 1045-1046, 1967.

[5] ALBANO, E. and RODDEN, W. P., "A Doublet-Lattice Method for Calculating Lift Distributions on Oscillating Surfaces in Subsonic Flows", *AIAA Journal*, Vol. 7, N. 2, pp. 279-285, 1969.

[6] DAT, R. and MALFOIS, J. P., " Sur le Calcul du Noyau de l'Equation Integrale de la Surface Portante en Ecoulement Subsonique Instationaire", *La Recherche Aérospatiale*, N. 5, pp. 251-259, 1970.

[7] DEMARAIS, R. N., "An Accurate and Efficient Method for Evaluating the Kernel of the Integral Equation Relating Pressure to Normalwash in Unsteady Potential Flow", AIAA Paper 82-0687, 1982.

[8] BISMARCK-NASR, M. N., "Kernel Function Occurring in Subsonic Unsteady Potential Flow", *AIAA Journal*, Vol. 29, N. 6, pp. 878-879, 1991.

[9] BISMARCK-NASR, M. N., "Kernel Function Occurring in Supersonic Unsteady Potential Flow", *AIAA Journal*, Vol. 29, N. 11, pp. 2006-2007, 1991.

[10] WATSON, G. N., *A Treatise on the Theory of Bessel Functions*, 2nd ed., Cambridge University Press, Cambridge, 1945.

[11] ABRAMOWITZ, M. and STEGUN, I. A. (Ed.), *Handbook of Mathematical Functions with Formulas, Graphs, and Mathematical Tables*, US Department of Commerce, 1964.

[12] ERDELYI, A. (Ed.), *Tables of Integral Transforms*, McGraw-Hill, New York, 1954.

ÍNDICE / CONTENTS